PROCEEDINGS A

royalsocietypublishing.org/journal/rspa

Research

Cite this article: Pacheco-Vega A, Sen M. 2025 Analytical and numerical steady states for thermal convection in an inclined, slender, two-dimensional enclosure. *Proc. R. Soc. A* **481**: 20250253.
https://doi.org/10.1098/rspa.2025.0253

Received: 27 March 2025
Accepted: 31 July 2025

Subject Areas:
mechanical engineering, applied mathematics, fluid mechanics

Keywords:
thermal convection, buoyancy, instability, enclosures

Author for correspondence:
Arturo Pacheco-Vega
e-mail: apacheco@calstatela.edu

Analytical and numerical steady states for thermal convection in an inclined, slender, two-dimensional enclosure

Arturo Pacheco-Vega[1] and Mihir Sen[2]

[1]Department of Mechanical Engineering, California State University-Los Angeles, Los Angeles, CA 90032, USA
[2]Department of Aerospace and Mechanical Engineering, University of Notre Dame, Notre Dame, IN 46556, USA

AP-V, 0000-0003-0566-6074; MS, 0000-0002-5136-7940

The present study considers uni- and multi-cellular natural convection of air in an inclined, slender, two-dimensional, rectangular enclosure, with emphasis on the existence of multiple steady states. The enclosure is subjected to a uniform heat flux along the long sidewalls and adiabatic conditions at the short-end walls. A mathematical model, based on the two-dimensional conservation equations under laminar flow and steady-state conditions, along with the Boussinesq approximation, is first formulated using non-dimensional stream function, vorticity and temperature, and then solved analytically and numerically, for different inclination angles, Rayleigh numbers and aspect ratios. The analytical solution, derived via the parallel-flow approximation, is used to describe the fluid flow and heat transfer in the core region, while detailed flow and temperature distributions are computed by finite difference approximations. By considering the cases of variable inclination angles for a fixed aspect ratio and different aspect ratios in a horizontal enclosure, the results reveal the emergence of multiple steady-state solutions for supercritical Rayleigh numbers around the horizontal configuration. Close agreement between numerical and analytical results confirms the robustness of the approach and provides insights into convective heat transfer mechanisms, including the influence of aspect ratio on the evolution of the steady states in horizontal enclosures.

Electronic supplementary material is available online at https://doi.org/10.6084/m9.figshare.c.8012258.

THE ROYAL SOCIETY PUBLISHING

1. Introduction

Natural convection in enclosures has been a subject of significant interest in fluid dynamics and heat transfer due to widespread occurrence in both natural and engineered systems [1–4]. This thermal transport process, driven by buoyancy forces resulting from temperature-induced density differences within a fluid, plays a crucial role in various environmental, engineering and commercial applications. These include atmospheric and oceanic circulation processes, heating, ventilation, and air conditioning systems, electronic cooling, solar energy collection, water desalination and energy-efficient building designs, among others [5–10]. In each of these cases, natural convection governs fluid transport mechanisms in either steady-state or transient conditions, which directly influence design considerations and operational performance critical for climate modelling, weather prediction, thermal regulation and energy efficiency. This mode of energy transfer is particularly important in enclosures, where the heat rate is regulated through walls/boundaries, making it highly sensitive to specific geometric configurations, boundary conditions and even thermal properties, all of which can shape the resulting convective patterns.

Extensive research has explored natural convection in enclosures using both analytical and numerical methodologies to understand fundamental behaviour and to implement it in practical applications. Though analytical studies have provided insights into the onset of convection, stability mechanisms and boundary-layer development in simple geometries [11–16], numerical simulations of the nonlinear incompressible fluid mechanics equations have been essential for capturing complex flow dynamics in a variety of enclosure geometries, boundary conditions, types of fluids and external forces such as magnetic fields or gravity modulation [3,9,10,17–25]. Despite the extensive body of work on natural convection in enclosures, the specific case of inclined, slender, two-dimensional enclosures remains a challenging topic due to the complexity resulting from the strong interplay not only between geometry and boundary conditions but also with orientation relative to gravity, which often leads to intricate and unexpected flow patterns. Previous studies on inclined enclosures with opposing isothermal walls, or rectangular cavities with uniform heat flux boundary conditions, have shown that the interactions among geometrical and operational parameters induce multiple steady states, bifurcations or symmetry-breaking instabilities [26–37].

An analytical approach frequently used to study thermal natural convection in slender enclosures relies on the assumption of unicellular convective motion, akin to a Hadley cell in atmospheric circulation. This methodology allows the problem to be simplified by applying a parallel-flow approximation to transform the governing partial differential equations (PDEs) into ordinary differential equations (ODEs) [16,38,39]. Based on this framework, early investigations by Vasseur *et al.* [40] examined the unicellular convective motion of a viscous fluid in an inclined layer, later extending their analysis to a composite enclosure containing a very thin conductive separation wall [41]. Additional research has further refined the parallel-flow approximation for both porous [42–45] and non-porous media [46–48], offering valuable insights into the stability and multiplicity of unicellular convective solutions in slender enclosures.

The present study considers uni- and multi-cellular thermal natural convection of air in an inclined, slender, two-dimensional, rectangular enclosure, subjected to uniform heat flux along the long sidewalls and adiabatic conditions at the short-end walls. The main focus is on the existence of multiple steady states and the influence that inclination angle and aspect ratio have on the thermal convection process in these systems. To this end, an integrated approach is adopted by combining an analytical technique, based on the parallel-flow approximation that enables closed-form solutions of the governing equations, with comprehensive numerical simulations to visualize and quantify the fluid flow and heat transfer characteristics. The paper is organized as follows: first, a brief description of the system and its mathematical formulation, in both dimensional and non-dimensional forms, is presented. This is followed by an overview of the numerical technique, including the computational domain and grid-independence tests. The development of the analytical approach within the framework of the parallel-flow approximation is then described and verified numerically. The two methods are subsequently applied to examine

royalsocietypublishing.org/journal/rspa Proc. R. Soc. A 481: 20250253

the effects of inclination angle and aspect ratio on the emergence of multiple steady states, for which two specific cases are considered: (1) a fixed aspect ratio with varying inclination angles and (2) a fixed inclination angle with different aspect ratios. Finally, the study provides a summary of key findings, including a potential mechanism by which steady states evolve with aspect ratio, and their implications for future research.

2. Problem description and mathematical formulation

We consider the fluid motion in a slender enclosure due to temperature-driven buoyancy forces. The enclosure, schematically illustrated in figure 1, has a height H and a length L, is filled with a Newtonian fluid and is inclined at an angle ϕ with respect to the horizontal. Energy exchanges in the enclosure occur via a constant heat flux through its long walls, while its short walls are adiabatic. For this system, the steady-state, incompressible equations for laminar flow, in the context of natural convection, are given by

$$\text{continuity} \quad \frac{\partial \hat{u}}{\partial \hat{x}} + \frac{\partial \hat{v}}{\partial \hat{y}} = 0, \tag{2.1a}$$

$$x\text{-momentum} \quad \hat{u}\frac{\partial \hat{u}}{\partial \hat{x}} + \hat{v}\frac{\partial \hat{u}}{\partial \hat{y}} = -\frac{1}{\rho}\frac{\partial \hat{p}}{\partial \hat{x}} + \nu\left(\frac{\partial^2 \hat{u}}{\partial \hat{x}^2} + \frac{\partial^2 \hat{u}}{\partial \hat{y}^2}\right) + \frac{1}{\rho}\hat{f}_x \tag{2.1b}$$

and

$$y\text{-momentum} \quad \hat{u}\frac{\partial \hat{v}}{\partial \hat{x}} + \hat{v}\frac{\partial \hat{v}}{\partial \hat{y}} = -\frac{1}{\rho}\frac{\partial \hat{p}}{\partial \hat{y}} + \nu\left(\frac{\partial^2 \hat{v}}{\partial \hat{x}^2} + \frac{\partial^2 \hat{v}}{\partial \hat{y}^2}\right) + \frac{1}{\rho}\hat{f}_y, \tag{2.1c}$$

where $\hat{u}$ and $\hat{v}$ are the fluid velocities in the $\hat{x}$- and $\hat{y}$-directions, respectively, $\hat{p}$ is pressure, $\hat{f}_x = \hat{f}\sin\phi$ and $\hat{f}_y = \hat{f}\cos\phi$ are the corresponding buoyancy forces in the $\hat{x}$- and $\hat{y}$-directions, and ν is the fluid kinematic viscosity. The symbol ($\hat{}$) indicates dimensional quantities. Using the Boussinesq approximation, the fluid buoyant force is given as $\hat{f} = \rho\hat{g}\beta(\hat{T} - \hat{T}_{ref})$, where $\hat{T}$ is its temperature, ρ is its density at a reference temperature $\hat{T}_{\text{ref}}$, $\hat{g}$ is the acceleration due to gravity and β is the corresponding coefficient of thermal expansion. The energy equation is given as

$$\hat{u}\frac{\partial \hat{T}}{\partial \hat{x}} + \hat{v}\frac{\partial \hat{T}}{\partial \hat{y}} = \alpha\left(\frac{\partial^2 \hat{T}}{\partial \hat{x}^2} + \frac{\partial^2 \hat{T}}{\partial \hat{y}^2}\right), \tag{2.1d}$$

where $\alpha = k/\rho c_p$ is the fluid thermal diffusivity, k is the thermal conductivity and c_p is its specific heat.

The corresponding boundary conditions are defined, mathematically, as

$$\text{short-end walls:} \quad \hat{x} = \pm\frac{L}{2}, \quad -\frac{H}{2} \le \hat{y} \le \frac{H}{2}, \quad \hat{u} = \hat{v} = 0, \quad \frac{\partial \hat{T}}{\partial \hat{x}} = 0 \tag{2.2a}$$

and

$$\text{long side walls:} \quad -\frac{L}{2} \le \hat{x} \le \frac{L}{2}, \quad \hat{y} = \pm\frac{H}{2}, \quad \hat{u} = \hat{v} = 0, \quad \frac{\partial \hat{T}}{\partial \hat{y}} = -\frac{\hat{q}}{k}, \tag{2.2b}$$

where $\hat{q}$ is the heat influx/eflux per unit length.

By using a normalization defined as follows:

$$x = \frac{\hat{x}}{H}; \quad y = \frac{\hat{y}}{H}; \quad u = \frac{\hat{u}}{\alpha/H}; \quad v = \frac{\hat{v}}{\alpha/H}; \quad p = \frac{\hat{p}}{\rho\alpha^2/H^2};$$

and

$$\theta = \frac{\hat{T} - \hat{T}_{\text{ref}}}{\hat{q}H/k}; \quad Pr = \frac{\nu}{\alpha}; \quad Ra = \frac{\hat{g}\beta\hat{q}H^4}{\nu\alpha k},$$

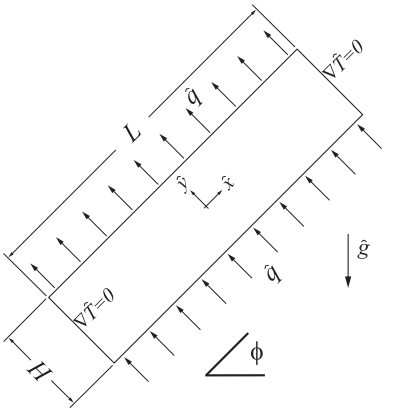

Figure 1. Natural convective flow in a slender cavity of aspect ratio $A = L/H$.

the non-dimensional versions of the set of equations (2.1*a*)–(2.1*d*) become

$$\frac{\partial u}{\partial x} + \frac{\partial v}{\partial y} = 0, \tag{2.3a}$$

$$u\frac{\partial u}{\partial x} + v\frac{\partial u}{\partial y} = -\frac{\partial p}{\partial x} + Pr\left(\frac{\partial^2 u}{\partial x^2} + \frac{\partial^2 u}{\partial y^2}\right) + RaPr\,\theta\sin\phi, \tag{2.3b}$$

$$u\frac{\partial v}{\partial x} + v\frac{\partial v}{\partial y} = -\frac{\partial p}{\partial y} + Pr\left(\frac{\partial^2 v}{\partial x^2} + \frac{\partial^2 v}{\partial y^2}\right) + RaPr\,\theta\cos\phi \tag{2.3c}$$

and

$$u\frac{\partial \theta}{\partial x} + v\frac{\partial \theta}{\partial y} = \frac{\partial^2 \theta}{\partial x^2} + \frac{\partial^2 \theta}{\partial y^2}. \tag{2.3d}$$

Since this is a two-dimensional flow system, we can use the stream function $\psi = \psi(x, y)$ and the vorticity $\omega = \omega(x, y)$, defined by

$$u = \frac{\partial \psi}{\partial y}; \quad v = -\frac{\partial \psi}{\partial x}; \quad \omega = \frac{\partial v}{\partial x} - \frac{\partial u}{\partial y},$$

to reduce equations (2.3*a*)–(2.3*c*) to a Poisson equation:

$$\frac{\partial^2 \psi}{\partial x^2} + \frac{\partial^2 \psi}{\partial y^2} + \omega = 0 \tag{2.4a}$$

and a single momentum transport equation,

$$\frac{\partial \psi}{\partial y}\frac{\partial \omega}{\partial x} - \frac{\partial \psi}{\partial x}\frac{\partial \omega}{\partial y} = Pr\left(\frac{\partial^2 \omega}{\partial x^2} + \frac{\partial^2 \omega}{\partial y^2}\right) + RaPr\left(\frac{\partial \theta}{\partial x}\cos\phi - \frac{\partial \theta}{\partial y}\sin\phi\right), \tag{2.4b}$$

with the energy equation (2.3*d*) becoming

$$\frac{\partial \psi}{\partial y}\frac{\partial \theta}{\partial x} - \frac{\partial \psi}{\partial x}\frac{\partial \theta}{\partial y} = \frac{\partial^2 \theta}{\partial x^2} + \frac{\partial^2 \theta}{\partial y^2}. \tag{2.4c}$$

Equations (2.4*a*), (2.4*b*) and (2.4*c*) provide the expressions for the three unknowns $\psi(x, y)$, $\omega(x, y)$ and $\theta(x, y)$, respectively, with the boundary conditions being now defined as

$$\text{short-end walls:} \quad x = \pm\frac{A}{2}, \quad -\frac{1}{2} \le y \le \frac{1}{2}, \quad \frac{\partial \psi}{\partial x} = \frac{\partial \psi}{\partial y} = 0, \quad \frac{\partial \theta}{\partial x} = 0 \tag{2.5a}$$

and

$$\text{long side walls:} \quad -\frac{A}{2} \le x \le \frac{A}{2}, \quad y = \pm\frac{1}{2}, \quad \frac{\partial \psi}{\partial x} = \frac{\partial \psi}{\partial y} = 0, \quad \frac{\partial \theta}{\partial y} = -1, \tag{2.5b}$$

where $A = L/H$ is the aspect ratio of the enclosure. It can be noted that the transformation

$$\phi \to -\phi, \quad \psi \to -\psi, \quad \theta \to -\theta, \quad x \to -x, \quad y \to -y,$$

neither alters the governing equations (2.4) nor the boundary conditions (equations (2.5)), and as it will be shown in the next sections, from the corresponding results, this symmetry is evident and consistent with the multiple physical scenarios of the problem.

The complete stream function and temperature fields can be obtained by solving the governing equations (2.4*a*)–(2.4*c*) and boundary conditions (2.5*a*) and (2.5*b*). Here, we explore their solution both numerically and analytically (by considering a parallel-flow approximation).

3. Numerical technique and grid independence

The two-dimensional set of equations (2.4) was discretized on a rectangular computational domain using finite difference approximations. Since typical iterative solutions of the elliptic equations, particularly those for the linear momentum and energy, are computationally expensive, equations (2.4*b*) and (2.4*c*) are modified by adding a transient term on the left-hand side to enable a marching solution via the method of false transient [49]. The spatial coordinates were discretized using central differences on a uniform grid, whereas a forward difference approximation was used for the transient terms. Integration of equations (2.4*b*) and (2.4*c*) is performed using an explicit solution algorithm with a time step of $\Delta t = 1 \times 10^{-5}$, which is sufficiently small to ensure stable results (although other methods, e.g. the alternating direction implicit procedure, could also be used to reduce even more the CPU times for the calculations). The Poisson equation, equation (2.4*a*), was solved using the successive overrelaxation technique. The stream function, temperature and vorticity fields are integrated until a steady state is reached, and convergence in the iterative procedure is achieved to within 10^{-3}%.

To ensure that the results are independent of the mesh size, a series of tests were carried out by employing coarser and finer grids for different values of aspect ratio A, Rayleigh number Ra and Prandtl number Pr. Assessment of the grid size on the results is carried out by evaluating the stream function at the centre of the enclosure, i.e. $\psi_c = \psi(0,0)$, which is used to characterize the intensity of the convective motion, and the local Nusselt number at the $x = 0$ section (central vertical line), for characterizing the convective heat transfer, defined [31] as

$$Nu = \frac{\hat{q}H}{k\Delta\hat{T}} = \frac{1}{\Delta\theta}, \tag{3.1}$$

where $\Delta\hat{T} = \hat{T}(0,-H/2) - \hat{T}(0,H/2)$ is the wall-to-wall temperature difference, and $\Delta\theta = \theta(0,-1/2) - \theta(0,1/2)$ is its non-dimensional form.

A typical example of these convergence tests is listed in table 1 for $A \in [3,20]$, $Ra \in [5 \times 10^4, 2.5 \times 10^5]$, $\phi = 0^\circ$ (which provides the strongest buoyant forces on the fluid) and $Pr = 0.72$. Although additional tests were performed for $Ra \in [10^3, 10^4]$, the results are not included in the table since, regardless of the value of A, they converge to the same values of ψ_c and Nu, for all mesh sizes considered. Note that the negative values of ψ_c, in the table, are associated with a clockwise rotation of the flow at the centre of the enclosure, whereas the positive ones correspond to its counterclockwise rotation, both of which are possible, as illustrated qualitatively in figure 2, in terms of the streamlines and isotherms for the sample case of $A = 3$, with $Ra = 5 \times 10^4$ and $\phi = 0^\circ$. Such symmetry in the fluid rotations reflects an inherent physical property of the system, which can be perceived by an observer either standing in front or behind the enclosure. Thus, from table 1, it can be observed that for $A = 3$, $Ra = 5 \times 10^4$ and $Ra = 10^5$, the coarser grid of 136×34 is sufficient to achieve accurate results. However, as A and/or Ra increase, as expected, smaller grids are necessary. For instance, for $A = 10$ and $Ra = \{5 \times 10^4, 10^5\}$, a grid size of 204×51 is now required. Finally, for $A = 20$, and the same values of Ra as before, only the finest mesh of 272×68 is sufficiently accurate. Note that for $Ra = 2.5 \times 10^5$, only the smallest grid size provides the required accuracy, independently of the value of A. From these tests, it was determined that a grid of 272×68, which provides a mesh size of $\Delta x = 0.07$ and $\Delta y = 0.015$, is sufficient and

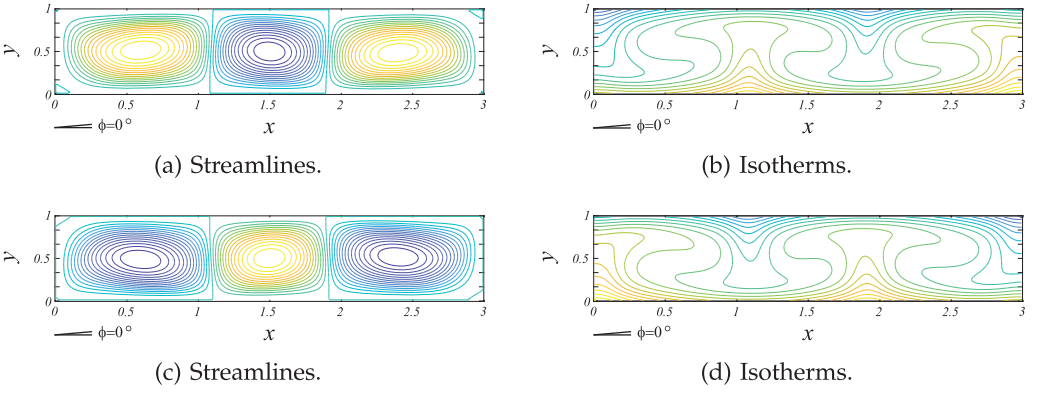

(a) Streamlines. (b) Isotherms.

(c) Streamlines. (d) Isotherms.

Figure 2. (a,c) Streamlines and (b,d) isotherms for $A = 3$, $Ra = 5 \times 10^4$ and $\phi = 0^\circ$. In left-hand figures, counterclockwise flow (yellow/green; lighter colour represents higher value) and clockwise flow (blue; darker colour represents higher value). In right-hand figures, lighter colour represents a higher temperature, while darker colour represents a lower temperature.

Table 1. Grid-independence tests for different aspect ratios A, $\phi = 0^\circ$ and Rayleigh numbers Ra.

grid size		136 × 34		204 × 51		272 × 68	
		ψ_c	Nu	ψ_c	Nu	ψ_c	Nu
$A = 3$							
Ra	5×10^4	−11.26	4.15	−11.21	4.11	−11.17	4.10
	10^5	14.48	4.85	14.51	4.80	14.50	4.78
	2.5×10^5	27.52	4.01	−31.23	5.08	−29.01	3.67
$A = 10$							
Ra	5×10^4	−8.82	3.27	−9.20	3.84	−11.99	4.18
	10^5	17.52	3.27	−18.39	3.51	−17.64	3.52
	2.5×10^5	30.33	3.06	28.13	4.13	−29.56	3.63
$A = 20$							
Ra	5×10^4	−10.86	4.17	10.66	4.08	10.95	4.09
	10^5	−14.11	5.02	14.52	4.84	17.80	3.31
	2.5×10^5	26.28	4.62	21.37	5.94	−19.86	5.47

therefore adopted in this investigation. To further verify grid independence of the numerical solution, we performed an additional simulation using an even finer mesh of 340 × 85. The results showed that, under the specified conditions, full convergence was achieved, with variations in Nu remaining, in general, below 3%.

4. Approximate analytical approach

Although numerical solutions provide a detailed account of the field quantities, like velocity and temperature, analytical solutions enable general analyses and can supplement the numerical information by, for instance, providing guidance onto which values of the parameters should be considered for the simulations.

(a) Mathematical model

For slender enclosures, i.e. those with large A, the flow in the central part of the cavity can be assumed to be parallel, such that $u = u(y)$ and $v = 0$. This assumption is in agreement with the

results reported by Bejan & Tien [38], Vasseaur *et al.* [40,41], Sen *et al.* [42] and Lamsaadi *et al.* [47], among others, for this and other similar systems, all of them in the context of *unicellular* convection patterns. Here, we follow these earlier works for the development of the mathematical formulation.

Given that the total flow rate at any x-section of the enclosure is zero, i.e.

$$0 = \int_{-1/2}^{1/2} \frac{\partial \psi}{\partial y}\, \mathrm{d}y = \psi|_{y=1/2} - \psi|_{y=-1/2},$$

it can be seen that the walls of the cavity are a streamline, and we can arbitrarily take $\psi = 0$ at $y = \pm 1/2$. Similarly, the energy flux integral at any x-section is given as

$$\int_{-1/2}^{1/2} \left(\frac{\partial \psi}{\partial y}\theta - \frac{\partial \theta}{\partial x} \right) \mathrm{d}y = 0, \tag{4.1}$$

since the total heat transported across any transversal section is also zero.

Let us take

$$\psi = \psi(y) \quad \text{and} \quad \theta = Cx + \eta(y), \tag{4.2}$$

where C is an unknown real constant—corresponding to the temperature gradient in the x-direction—with η being the variation of temperature in the y-direction. The governing equations (2.4) are transformed into the following set of ODEs:

$$\frac{\mathrm{d}^4 \psi}{\mathrm{d}y^4} + Ra \, \sin\phi \frac{\mathrm{d}\eta}{\mathrm{d}y} = Ra\, C \cos\phi \tag{4.3a}$$

and

$$\frac{\mathrm{d}^2 \eta}{\mathrm{d}y^2} - C\frac{\mathrm{d}\psi}{\mathrm{d}y} = 0, \tag{4.3b}$$

which are independent of the Prandtl number Pr.

The total order of the differential equation set, i.e. equations (4.3), plus the constant C in them provides a total of seven constants to be determined. There are also seven conditions, namely, the integral relation, equation (4.1), rewritten as

$$\int_{-1/2}^{1/2} \left([Cx + \eta(y)] \frac{\mathrm{d}\psi}{\mathrm{d}y} - C \right) \mathrm{d}y = 0, \tag{4.4}$$

four boundary conditions for ψ,

$$y = \pm\frac{1}{2}, \quad \psi = 0, \quad \frac{\partial \psi}{\partial y} = 0 \tag{4.5}$$

and two for η as

$$\frac{\partial \eta}{\partial y} = -1 \quad \text{at} \quad x, y = \pm\frac{1}{2}. \tag{4.6}$$

Note that since the two boundary conditions for η are equivalent, only one can be used, and an additional condition is—therefore—needed. Thus, by taking into account the symmetry of the problem, the following condition:

$$\eta = 0 \quad \text{at} \quad x = 0, \quad y = 0 \tag{4.7}$$

can be used to supplement equation (4.6) and compute the final constant in the mathematical model.

(b) Analytical solution for arbitrary inclination angle

There are two special cases that will be considered in a separate manner, namely, $C\sin\phi > 0$ and $C\sin\phi < 0$. The corresponding final solutions are provided next and, in some detail, in appendix A.

(i) Natural solution, $C \sin\phi > 0$

This case corresponds to having C and $\sin\phi$, either both positive or both negative. In the former case ($C > 0$, $\phi > 0$), the $x = A/2$ end is hotter and motion is counterclockwise, while in the latter ($C < 0$, $\phi < 0$), the $x = -A/2$ end is hotter and motion is clockwise. In either case, the motion is the one that would result from rest and a conductive temperature field. Here, this will be referred to as the *natural* solution since the fluid *rises* as its temperature increases.

The solution to equation (4.3*a*), with boundary conditions (equation (4.5)), is

$$\psi(y) = -\frac{P_B}{2e}\left[(1-\epsilon)\left\{\sin\frac{e}{2}\,\sinh\frac{e}{2} - \sin ey\,\sinh ey\right\} + (1+\epsilon)\left\{\cos\frac{e}{2}\,\cosh\frac{e}{2} - \cos ey\,\cosh ey\right\}\right], \tag{4.8}$$

where P_B is unknown at this point, and

$$e = \left(\frac{Ra\,C}{4}\sin\phi\right)^{1/4} \quad \text{and} \quad \epsilon = \cot\frac{e}{2}\,\tanh\frac{e}{2}. \tag{4.9}$$

On the other hand, the solution to equation (4.3*b*) with conditions equations (4.6) and (4.7) is

$$\eta(y) = \frac{CP_B}{2e^2}\{\sin ey\,\cosh ey + \epsilon\cos ey\,\sinh ey\} + Cy\,\cot\phi, \tag{4.10}$$

with the parameter P_B being

$$P_B = -\frac{2e(1 + C\cot\phi)}{C\{(1+\epsilon)\cos(e/2)\cosh(e/2) + (1-\epsilon)\sin(e/2)\sinh(e/2)\}}. \tag{4.11}$$

Finally, to obtain an equation for the constant C, condition equation (4.4) is used to give

$$\begin{aligned}&\frac{CP_B^2}{16e^3}[(\epsilon^2 + 2\epsilon - 1)\cos e\,\sinh e + (-\epsilon^2 + 2\epsilon + 1)\sin e\,\cosh e] - \frac{\epsilon CP_B^2}{4e^2}\\ &+ \frac{CP_B\cot\phi}{2e}\left[(1-\epsilon)\sin\frac{e}{2}\,\sinh\frac{e}{2} + (1+\epsilon)\cos\frac{e}{2}\,\cosh\frac{e}{2}\right]\\ &- \frac{CP_B\cot\phi}{e^2}\left[\epsilon\cos\frac{e}{2}\,\sinh\frac{e}{2} + \sin\frac{e}{2}\,\cosh\frac{e}{2}\right] - C = 0.\end{aligned} \tag{4.12}$$

The resulting transcendental equations (4.9), (4.11) and (4.12) have to be simultaneously solved for the unknowns e, P_B and C. This is done numerically using a Newton–Raphson scheme and, since it is always possible to find real values of the constants for any Ra and ϕ, the stream function and temperature fields are then known from equations (4.8) and (4.10).

(ii) Antinatural solution, $C \sin\phi < 0$

This scenario, on the other hand, will be the *antinatural* solution since the fluid *falls* as its temperature increases. This solution, although not immediately intuitive, has been observed experimentally in several systems, including natural convection loops [33]. In such a case, C and $\sin\phi$ have opposite signs. For positive inclinations ($\phi \geq 0$), the motion is clockwise and the $x = -A/2$ end is hotter. For negative inclinations ($\phi < 0$), the motion is counterclockwise and the $x = A/2$ end is hotter. In either case, this motion—whether experimentally or numerically—cannot start from rest conditions with a conductive temperature field. In fact, it is opposite in direction to the natural motion illustrated in §4b(i).

The stream function, from equation (4.3*a*), with conditions equation (4.5), is now given by

$$\psi(y) = \frac{P_D}{b}\left[\beta\left(\cos by - \cos\frac{b}{2}\right) + \left(\cosh by - \cosh\frac{b}{2}\right)\right], \tag{4.13}$$

where the parameters b and β are, respectively, given by

$$b = (-Ra\,C\sin\phi)^{1/4} \quad \text{and} \quad \beta = \frac{\sinh(b/2)}{\sin(b/2)}. \tag{4.14}$$

From equation (4.3*b*), along with conditions equations (4.6) and (4.7), we get

$$\eta(y) = \frac{CP_D}{b^2}(\beta \sin by + \sinh by) + Cy \cot\phi, \tag{4.15}$$

where the parameter P_D is given by

$$P_D = -\frac{b(1 + C\cot\phi)}{C(\beta \cos(b/2) + \cosh(b/2))}. \tag{4.16}$$

The energy flux integral condition equation (4.1) then provides the equation for C as

$$\frac{CP_D{}^2}{2b^3}(\beta^2 \sin b + \sinh b) - \frac{CP_D{}^2}{2b^2}(\beta^2 + 1) + \frac{CP_D \cot\phi}{b}\left(\beta \cos\frac{b}{2} + \cosh\frac{b}{2}\right) - \frac{2CP_D \cot\phi}{b^2}\left(\beta \sin\frac{b}{2} + \sinh\frac{b}{2}\right) - C = 0. \tag{4.17}$$

Again, a Newton–Raphson method is used to obtain the numerical values of C with which the stream function and temperature fields can be determined. Two sets of constants are obtained for a given Ra and ϕ. However, they are real only in a narrow range of angles around zero, for which antinatural steady states exist.

(c) Numerical verification tests

Since the analytical solutions above are valid for a substantially large aspect ratio A (i.e. $A \gg 1$), and the parallel-flow approximation is applicable only for the central part of the enclosure, a test is required to determine the smallest value of the aspect ratio for which the large-A approximation is close enough to the numerical solutions. To this end, we consider two special systems: a horizontal enclosure ($\phi = 0$) heated from below and a vertical cavity ($\phi = 90^\circ$) heated from the side, both of which are subsets of the general case of the inclined enclosure herein studied. For these systems, both their mathematical model—which reduces from equations (4.3*a*) and (4.3*b*)—and their corresponding analytical solutions are detailed in appendix A. Here, we discuss their results.

The corresponding results are presented in figures 3 and 4 for inclination angles $\phi = 0$ and $\phi = 90^\circ$, respectively, in terms of the stream function at the centre of the cavity ψ_c and the local Nusselt number at the vertical centreline across the long walls, Nu, being defined by equation (3.1). Two values of the Rayleigh number, namely, $Ra = 1 \times 10^4$ and $Ra = 5 \times 10^4$, and several enclosures with different aspect ratio A were considered. In both figures, the values computed from the numerical data, in the range of $A \in [0.25, 10]$, are illustrated as symbols, whereas those corresponding to the analytical solutions—from equation (A 13) for $\phi = 0$ and equations (A 17) and (A 19) for $\phi = 90^\circ$, in appendix A—are shown for $A \in [1, 10]$ as continuous horizontal lines. It is important to note that though the results are shown for $Pr = 0.72$, which corresponds to air, little difference was found for other Pr numbers for values outside the $A \in [1, 2]$ range.

From the figures, it can be observed that the results from the approximate analytical approach for both ψ_c and Nu, in the two sample cases, are close to those of the numerical simulations for an aspect ratio as small as $A = 2$, with those for $A \geq 4$ being—essentially—indistinguishable. This is further corroborated in figure 5, which shows the error in the approximation from the analytical model and the corresponding convergence of its results to those obtained numerically. From the figure, it can be seen that in the case of a cavity with an inclination angle $\phi = 0$, if the aspect ratio is small, e.g. $A = 2$, the associated error from the analytical model for ψ_c and Nu are 8.3% and 3.6%, respectively, for $Ra = 1 \times 10^4$ (with corresponding errors of 0.6% and 13.6% for $Ra = 5 \times 10^4$). On the other hand, if the enclosure has an aspect ratio of $A = 4$, the associated errors are bounded to only 0.5% and 2%, respectively, regardless of the Ra number. Similar trends are observed for cases in which the inclination angle is $\phi = 90^\circ$, but with even smaller errors. This indicates that the analytical approach may be applicable even in cases where the value of the aspect ratio A is

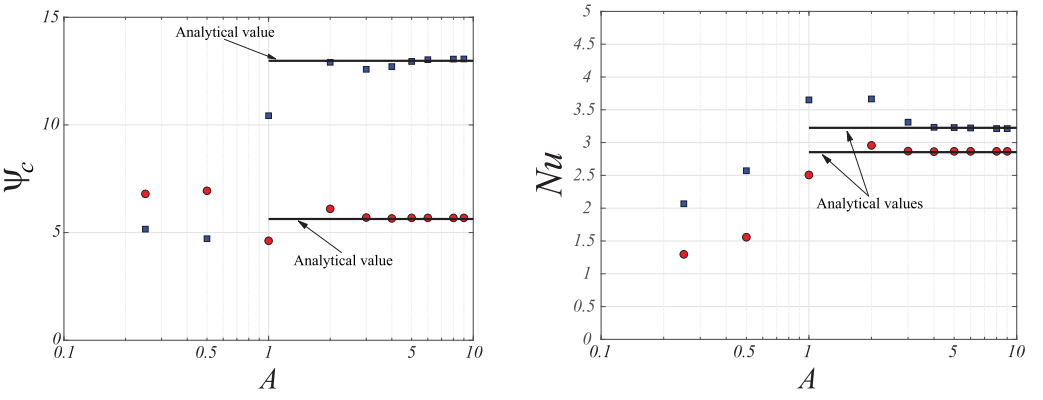

(a) ψ_c vs. A. (b) Nu vs. A.

Figure 3. Analytical versus numerical values of ψ_c and *Nu* for different values of A, $\phi = 0^\circ$ and $Pr = 0.72$. (●): $Ra = 1 \times 10^4$; (■): $Ra = 5 \times 10^4$.

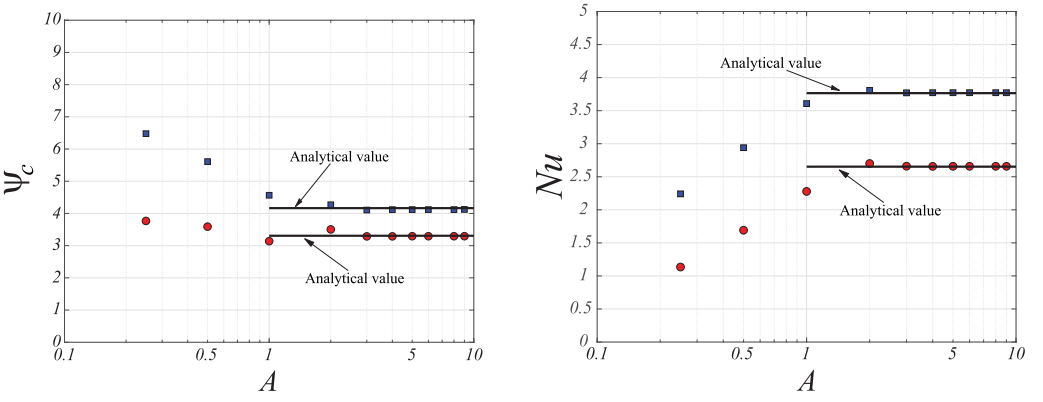

(a) ψ_c vs. A. (b) Nu vs. A.

Figure 4. Analytical versus numerical values of ψ_c and *Nu* for different values of A, $\phi = 90^\circ$ and $Pr = 0.72$. (●): $Ra = 1 \times 10^4$; (■): $Ra = 5 \times 10^4$.

not sufficiently large as to be considered a 'large-A approximation'. In that case, of course, there will be an approximation error from the analytical model associated with the aspect ratio of the enclosure to be analysed.

5. Multiplicity of solutions

From a mathematical point of view, the governing equations (2.4*a*)–(2.4*c*) may have a unique solution as an initial value problem. However, when the equations are associated with a boundary-value problem—the slender inclined cavity being a perfect example of it—multiple steady states are then possible. This is shown in the next sections for two different scenarios: (1) the case of an enclosure of constant aspect ratio A and varying inclination angle ϕ, and (2) a set of enclosures of different aspect ratio A, with a single inclination angle ϕ.

(a) Enclosure of fixed aspect ratio A and varying inclination angle ϕ

The enclosure considered for this analysis has an aspect ratio $A = 4$, which is sufficiently large to enable using the approximate analytical model of §4, and its solutions, along with the results

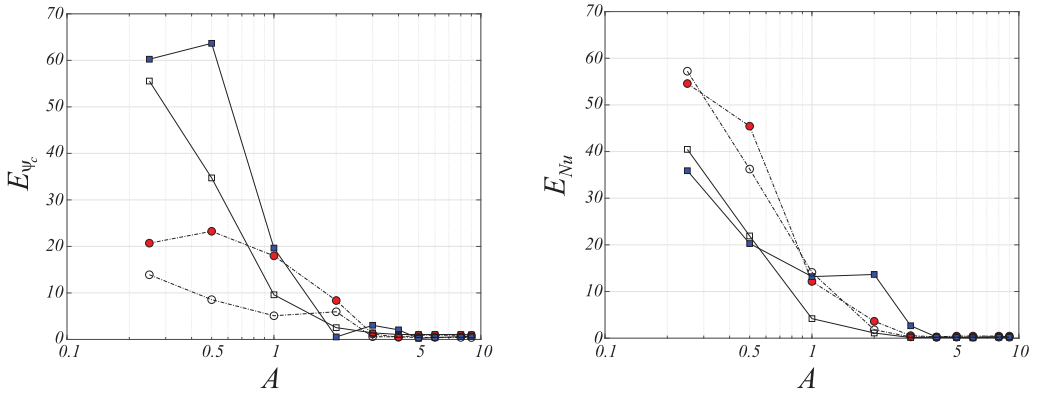

(a) E_{ψ_c} vs. A. (b) E_{Nu} vs. A.

Figure 5. Approximation error of the analytical approach for ψ_c and Nu, as a function of A. Solid symbols: $\phi = 0°$; Open symbols: $\phi = 90°$. (— ● —, — ○ —): $Ra = 1 \times 10^4$; (· — ■ — ·, · — □ — ·): $Ra = 5 \times 10^4$.

from the numerical method described in §3. The inclination angles are in the range of $-180° < \phi < 180°$, while the set of Rayleigh numbers considered, on the other hand, is confined to the range $Ra \in [720, 1 \times 10^5]$. The corresponding results from both techniques are presented in terms of the stream function at the centre ψ_c and the Nusselt number Nu, supplemented by detailed accounts of the numerically obtained streamlines and temperature fields inside the enclosure. Here, positive values of ψ_c represent counterclockwise rotations, while a negative value of ψ_c is associated with a clockwise motion of the flow, both at the centre of the enclosure.

Figure 6a,b presents the values of ψ_c and Nu, respectively, as functions of ϕ for different values of Ra. In both figures, continuous (and broken) lines illustrate analytical solutions, whereas the numerical data are displayed as symbols. Besides the excellent correspondence between the analytical and numerical results, from the figures, it can be observed that only one steady state exists for each inclination angle in the ranges $-180° < \phi < -\phi^*$ and $\phi^* < \phi < 180°$, whereas three different steady states are possible in the $-\phi^* < \phi < \phi^*$ range. Here, ϕ^* varies from $\phi^* = 0°$ when $Ra \leq 720$ to a maximum value of $\phi^* = 38.3°$ for $Ra = 1 \times 10^4$ (with specific values of $\phi^* = 25.5°$ for $Ra = 1 \times 10^5$ and $\phi^* = 33.5°$ for $Ra = 5 \times 10^4$). On looking closer, both figures clearly illustrate the symmetry of the problem and its corresponding governing equations, as noted in §2 and 3. From figure 6a, the stream function is symmetric with respect to the origin of the $\psi_c - \phi$ plane (the first and third quadrants showing natural flows, while the second and fourth quadrants illustrate the antinatural flows), whereas the Nusselt number, in figure 6b, shows a mirror image in relation to the vertical line $\phi = 0$ of the $Nu - \phi$ plane. In any case, from a physical perspective, the observed symmetry is an inherent property of the system, as previously noted, and can be perceived by an observer standing either in front of or behind the enclosure. However, regardless of the position of the observer, there are two possible values of the streamfunction at the centre of the enclosure ψ_c, corresponding to the two possible orientations of circulation—clockwise or counterclockwise—further illustrating the symmetric nature of the flow and temperature fields. It is to note that a similar type of behaviour has been predicted numerically [32,37] and experimentally observed [27] for flow in natural convection loops and in other related problems [40,42]. Further analysis of figure 6a shows that at $Ra = Ra_{cr} = 720$, which is the critical value of the Rayleigh number for this system, the $\psi_c(\phi)$ curve is single valued for all inclination angles except the origin, at which a point of inflexion—where the curve is tangent to the $\phi = 0°$ axis—arises. For $Ra > Ra_{cr}$, the profile of $\psi_c(\phi)$ becomes convoluted and the curve multi-valued, with the existence of three different steady states for inclinations in the range $-\phi^* < \phi < \phi^*$, as indicated above. A similar situation is also shown in figure 6b, for the $Nu(\phi)$ curves, which become multi-valued for $Ra \geq Ra_{cr}$, with a maximum value of Nu occurring at inclination angles between zero and 90°. From the figure, it can be noticed that for a given inclination angle ϕ, for small values of Ra, the

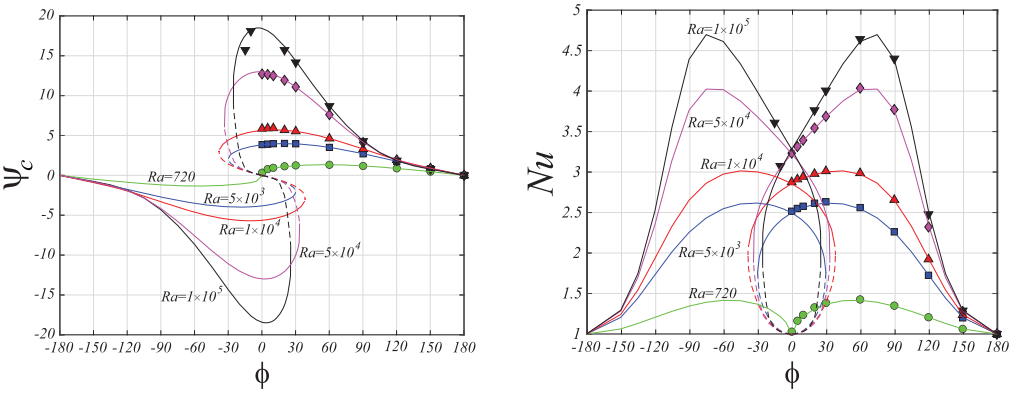

(a) ψ_c vs. ϕ. (b) Nu vs. ϕ.

Figure 6. Numerical and analytical values of ψ_c and Nu as functions of ϕ. Solid symbols correspond to numerical solutions; lines correspond to analytical solutions. (●): $Ra = 720$; (■): $Ra = 5 \times 10^3$; (▲): $Ra = 1 \times 10^4$; (♦): $Ra = 5 \times 10^4$; (▼): $Ra = 1 \times 10^5$. Broken lines are for unstable solutions.

Nusselt number is $Nu = 1$, since the temperature field is dominated by conduction; however, Nu increases substantially for larger values of Ra, as the temperature field becomes dominated by convection.

Stability characteristics of the steady states for both ψ_c and Nu can be deduced from the numerical information. The numerical method, it must be recalled, is based on integration in time and, as a consequence, the steady states—shown as symbols in the figures—thus obtained from it correspond to linearly stable states. The analytical approximation, on the other hand, applies equally to stable as well as unstable solutions. This is illustrated in figure 6a,b, which show that for some values of Ra, above Ra_{cr}, part of the outer branch of ψ_c and Nu, covering both natural and antinatural states, is stable. At a large enough Ra number, however, the entire branch becomes unstable. The inner antinatural branch, shown in both figures by broken lines, is unconditionally unstable, as numerical solutions could not be obtained for any point on this branch. As indicated above, this feature has also been observed, and reported, in other similar natural convection systems [32,33,37,40,42].

Further analysis of the multiplicity of steady states and their stability is carried out by observing figure 7a,b, which illustrate the values of ψ_c and Nu as functions of Ra, in the range of $Ra \in [0, 5 \times 10^3]$, for inclination angles $\phi = 0°$, 5°, 10° and 20°, all well within the aforementioned $[-\phi^*, \phi^*]$ range. As before, in both figures, analytical solutions are shown by lines, with the unstable part of the antinatural branch being displayed by broken lines, while the numerical confirmation of the stable solutions is specified by symbols. In figure 7a, for positive inclination angles ($\phi > 0$), natural circulation is indicated by a positive ψ_c (upper half of the figure), whereas the antinatural motion is represented by a negative value of ψ_c (lower half of the figure). In contrast, for the $Nu - Ra$ plot in figure 7b, the region of natural circulation extends to the left of the $\phi = 0$ curve, while the antinatural circulation comprises the area to the right of it. Importantly, in the case of negative inclination angles ($\phi < 0$), the sign of ψ_c in figure 7a will change; however, in agreement with the results of figure 6b, the values of the Nusselt number in figure 7b remain positive. For $\phi = 0°$, which corresponds to the horizontal enclosure, figure 7a shows that there is no motion possible up to the critical Rayleigh number, $Ra_{cr} = 720$, at which a bifurcation into two symmetrical counter-rotating convection states occurs. This gradual increase of the Ra number from zero would be equivalent to a heating process starting from a purely conductive temperature profile and rest conditions of the fluid; if $Ra < Ra_{cr}$, only one steady state exists but—independently of inclination angle ϕ—when $Ra \geq Ra_{cr}$, multiple states are possible. For $\phi > 0°$, the bifurcation diagram for ψ_c (and its related layout for Nu in figure 7b) changes considerably for any inclination angle. Thus, following the work of Sen *et al.* [42], we use the critical Rayleigh

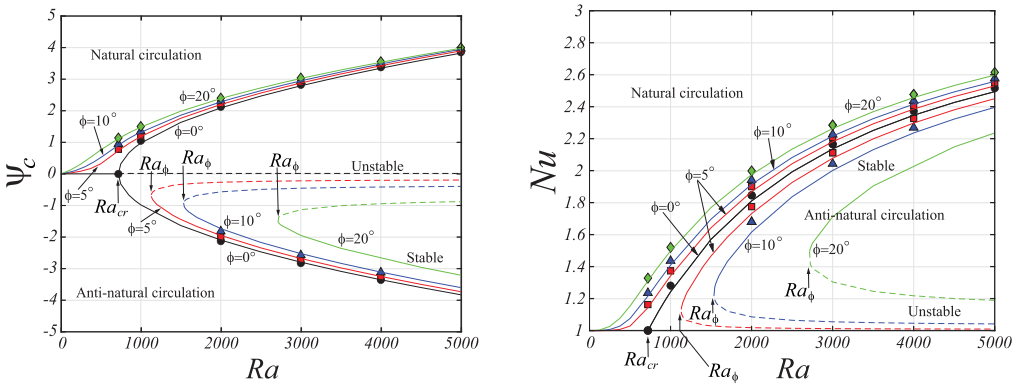

(a) ψ_c vs. Ra. (b) Nu vs. Ra.

Figure 7. Numerical and analytical values of ψ_c and *Nu* as functions of *Ra*. Solid symbols correspond to numerical solutions; lines correspond to analytical solutions. (●): $\phi = 0°$; (■): $\phi = 5°$; (▲): $\phi = 10°$; (♦): $\phi = 20°$. Broken lines are for unstable solutions.

number for the inclined enclosure Ra_ϕ, defined as the smallest value of Rayleigh number at which multiple steady states appear for an inclined cavity ($\phi > 0$), and notice in both figures that though the natural state exists for $\phi > 0$ (and $\phi < \phi^*$), the antinatural state appears only if $Ra > Ra_\phi$. Furthermore, as expected, the value of Ra_ϕ increases with increasing inclination angle ϕ; e.g. $Ra_\phi = 1135$ for $\phi = 5°$, $Ra_\phi = 1535$ for $\phi = 10°$ and $Ra_\phi = 2715$ for $\phi = 20°$. Finally, from figure 7b, it can be seen that, as anticipated, the antinatural states have a lower value of *Nu* than the corresponding natural states for the same inclination.

Numerically, any inclination would bias the convective solution, starting from rest flow conditions and purely conductive temperature profiles, towards the natural state. The antinatural state can be reached only through initial conditions different from rest and exists only if $Ra > Ra_\phi$. In such a case, the antinatural convective circulations are obtained by starting the calculations with the natural solution and then modifying the inclination gradually; i.e. the natural state of the previous angle is first used as a starting point in the computation, with the inclination angle being slightly adjusted to obtain the antinatural state. If the change of angle is sufficiently small, there is no change in the direction of the circulation patterns. This sequence is exemplified in the context of unicellular convection [40] in figure 8, for an enclosure of aspect ratio $A = 3$ and $Ra = 5 \times 10^4$, where streamlines and the corresponding isotherms are illustrated for inclination angles $\phi = 5°$, $\phi = 0°$ and $\phi = -5°$. From the figure, it can be noticed that, in all cases shown, by choosing appropriate initial conditions at the start of the computation, a single counterclockwise circulation of the fluid (as evident from the way the isotherms are curved) is obtained. In the figure, the top row figures for $\phi = 5°$ (figure 8a,b) are realized by starting from fluid at rest and a conductive temperature field; these are then used as initial states for the middle row figures illustrating the results for $\phi = 0°$ (figure 8c,d), which in turn are the initial conditions for the numerical results of the bottom row figures for $\phi = -5°$ (figure 8e,f). Further inspection of the inclination angle $\phi = -5°$ demonstrates that if the computations are started from rest conditions and conductive isotherms, then a set of clockwise unicellular circulation patterns, displayed in figure 9, develops. When these results are compared to the counterclockwise circulation cells of figure 8, which are obtained under identical spatial boundary conditions but different initial conditions, it is clear that not only multiplicity of steady solutions are possible but also the clockwise circulation of the fluid inside the cavity with inclination angle $\phi = -5°$ is the natural state. A similar conclusion can be reached for the case of $\phi = 0°$, by contrasting the unicellular convection patterns of figure 8, to the tricellular circulation structures of figure 2, which correspond to the antinatural and natural states, respectively. Note that although the same qualitative results could have been obtained with a value of $A = 4$, using an enclosure of aspect ratio $A = 3$ enables direct comparison between the

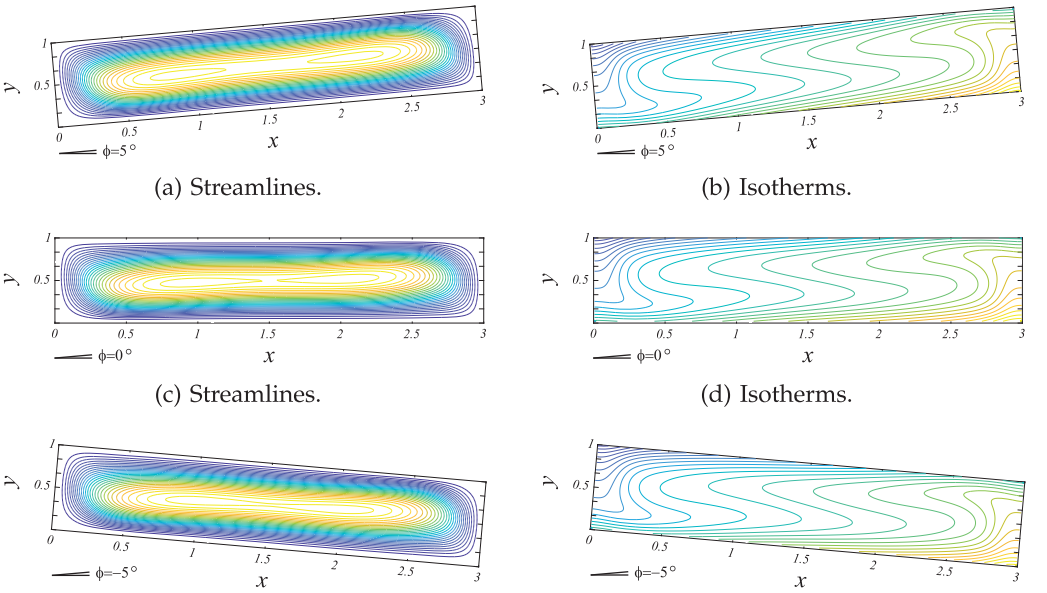

(a) Streamlines. (b) Isotherms.

(c) Streamlines. (d) Isotherms.

(e) Streamlines. (f) Isotherms.

Figure 8. Natural convection with unicellular counterclockwise flow. (a,c,e) Streamlines and (b,d,f) isotherms for $A = 3$, $Ra = 5 \times 10^4$ and three inclination angles. Top row: $\phi = 5^\circ$, with initial conditions of quiescent flow and conductive temperature field. Middle row: $\phi = 0^\circ$, and bottom row: $\phi = -5^\circ$, both use initial conditions taken from the natural solution at the previous angle with a slight angle adjustment.

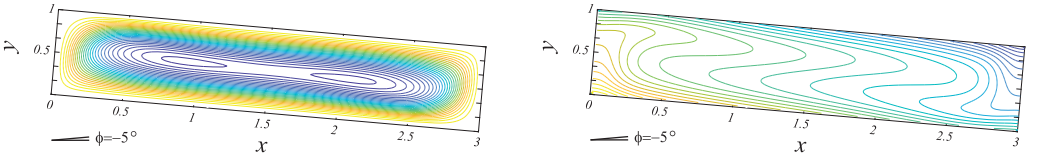

(a) Streamlines. (b) Isotherms.

Figure 9. Natural convection with unicellular clockwise flow. (a) Streamlines and (b) isotherms for $A = 3$, $Ra = 5 \times 10^4$ and $\phi = -5^\circ$, with initial conditions of quiescent flow and conductive temperature field.

numerical results of figure 8 to those of figure 2, all of which were obtained with the same spatial boundary conditions.

The two special cases of a horizontal ($\phi = 0^\circ$) and a vertical slender enclosure ($\phi = 90^\circ$), briefly discussed in §4c, are especially interesting. As noticed earlier from figures 6 and 7, the situation for $\phi = 0^\circ$ is the simplest for small Ra numbers, since below the critical $Ra < Ra_{cr} = 720$, the only stable solution is a conduction temperature field with the fluid at rest. The value $Ra_{cr} = 720$, at which the onset of convection occurs, is found to agree with the results of the linear stability theory, predicting a supercritical pitchfork bifurcation. For $Ra > Ra_{cr}$, there are three solutions, including an unstable one at rest, and two stable symmetrical clockwise and counterclockwise solutions at the centre of the enclosure [12]. As noted before, for inclinations $\phi \neq 0^\circ$, in particular $\phi = 90^\circ$, since the action of gravity is perpendicular to that of the heat flux, it is more difficult to show multiplicity of steady states, since the solutions are then not symmetric. However, upon calculating ψ_c and Nu, both numerically and using the equation models equations (A 7*a*) and (A 7*b*) for $\phi = 0^\circ$, and equations (A 14*a*) and (A 14*b*) for $\phi = 90^\circ$, in the range of Rayleigh numbers $Ra \in [100, 10^6]$, some general features can be identified. The corresponding results are shown as symbols and continuous lines, respectively, in figure 10, with figure 10a,b illustrating the values

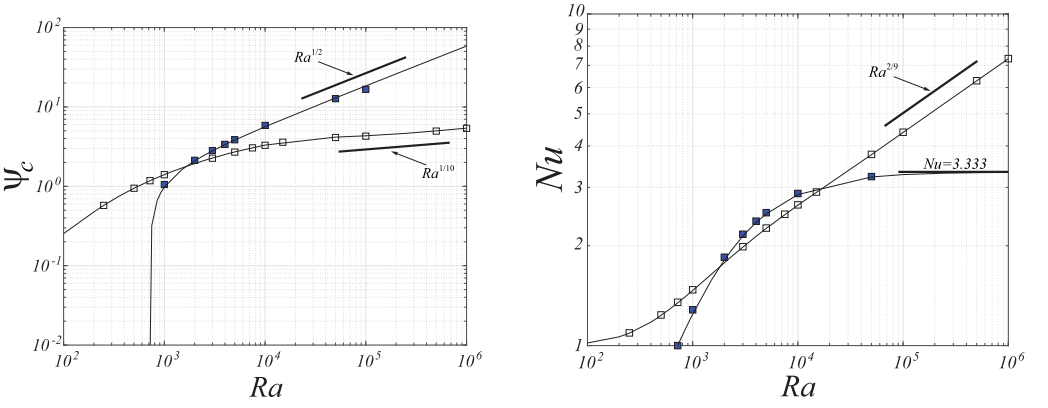

(a) ψ_c vs. Ra. (b) Nu vs. Ra.

Figure 10. Analytical and numerical values of $\psi_c(Ra)$ and $Nu(Ra)$ for $\phi = 0^\circ$ and $\phi = 90^\circ$. Symbols correspond to numerical data with $A = 4$ and $Pr = 0.72$. Lines are for analytical solutions. (■): $\phi = 0^\circ$; (□): $\phi = 90^\circ$.

of ψ_c and Nu as functions of the Rayleigh number. From the figures, we find that, as expected, for a given Ra, the strength of the fluid motion is larger for the horizontal enclosure since the strongest buoyancy force occurs at the inclination angle $\phi = 0^\circ$. The exception to this trend occurs in the range $Ra < Ra_{cr} = 720$, since motion of the fluid exists for $\phi = 90^\circ$, but not for $\phi = 0^\circ$. In the case of the Nusselt number Nu, the situation is slightly different since its values for $\phi = 0^\circ$ are only larger than those of $\phi = 90^\circ$ in the range $10^3 < Ra < 10^4$. As noticed before, for $\phi = 0^\circ$ and $Ra < Ra_{cr}$, there is pure conduction, while in the case of the vertical cavity, the heat transfer is dominated by convection. For large values of the Rayleigh number, for $\phi = 0^\circ$, the values of ψ_c increase as $Ra^{1/2}$, while those for $\phi = 90^\circ$, increase at the lower rate of $Ra^{1/10}$. On the other hand, for $\phi = 0^\circ$, the Nusselt number reaches an asymptotic value of $Nu = 3.333$, with both the analytical and numerical results presented here closely matching those reported in previous studies [40,41,46,47]. In contrast, for $\phi = 90^\circ$, Nu increases with Rayleigh number following a $Ra^{2/9}$ scaling, which corresponds well with the boundary-layer analysis by Kimura & Bejan [31], who proposed the correlation $Nu = 0.3402Ra^{2/9}$.

(b) Enclosure of different aspect ratios A and fixed inclination angle ϕ

For the analysis in this section, which is completely based on numerical computations of the model equations (2.4) and the boundary conditions equations (2.5), we consider a set of horizontal enclosures with aspect ratios in the range of $3 \le A \le 20$, with a fluid of Prandtl number $Pr = 0.72$ (air), and for a single value of Rayleigh number, $Ra = 5 \times 10^4$, which is well above Ra_{cr}. Note that we have selected the horizontal layout (for which inclination angle is $\phi = 0^\circ$), since the fluid in this configuration sustains the strongest buoyancy forces, and the system offers the largest set of steady states. As before, the solutions are presented both in terms of the value of the stream function at the centre of the enclosure ψ_c, and the Nusselt number Nu, across a vertical line, at $x = 0$, joining the two horizontal walls, being reinforced by comprehensive descriptions of the numerical data in terms of streamlines and temperature fields inside the enclosure, and by information on the number of developing convection structures N_{cells}, in each system. The analysis, which is divided into two parts, is first centred on the numerical results when the aspect ratio is increased from $A = 3$ to $A = 20$, whereas the second focuses on the solutions when decreasing A, from $A = 20$ to $A = 3$. For all the numerical simulations, the boundary conditions are those of equations (2.5). However, with the exception of the first computer run—for both $A = 3$ when increasing A, and $A = 20$ for the path of decreasing A—for which the set of initial conditions used is that of a conduction temperature field with the fluid being at rest, for all other runs, the numerical solutions of the previous value of A are used as the initial conditions for the

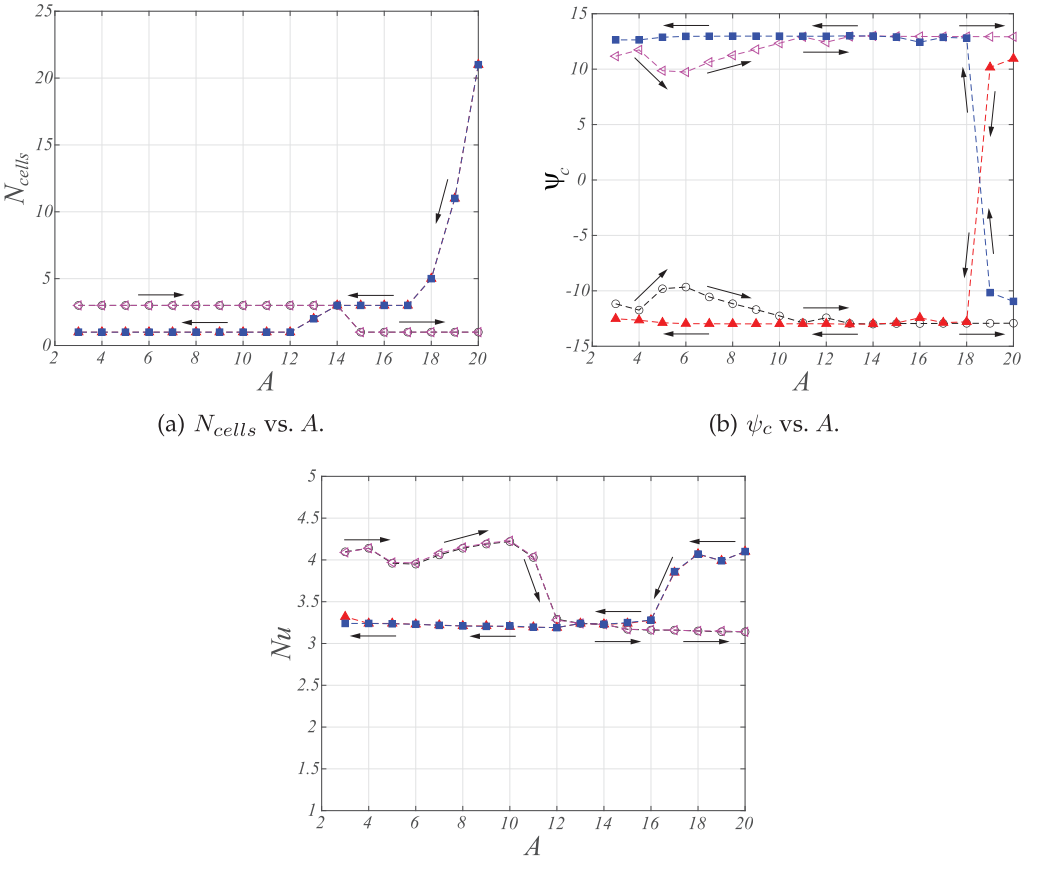

(a) N_{cells} vs. A. (b) ψ_c vs. A.

(c) Nu vs. A.

Figure 11. Numerical results of N_{cells}, ψ_c and Nu for $\phi = 0^\circ$ and $Ra = 5 \times 10^4$, over the range of $A \in [3, 20]$. Open symbols are for increasing A; filled symbols are for decreasing A. Black and red symbols represent solutions with a slightly positive angle, while blue and magenta indicate a slightly negative angle. The increasing-A and decreasing-A curves have been shifted horizontally by +5% and −5%, respectively, for clarity.

computations in an enclosure of the subsequent value of the aspect ratio. This procedure enables finding whether the steady-state solutions for a system with one value of the aspect ratio remain stable for a layout with another value.

Figure 11a–c shows, respectively, the values of N_{cells}, ψ_c and Nu, as functions of the aspect ratio A, in the range $A \in [3, 20]$, for $Ra = 5 \times 10^4$. In these three figures, open symbols correspond to the results obtained when A increases, while filled symbols represent those in which the path followed is that of decreasing A. For the stream function at the centre of the cavity ψ_c, positive values correspond to a counterclockwise rotation of the flow, whereas the negative ones are associated with clockwise rotations. As discussed earlier, the symmetry of the problem implies the existence of two equivalent, physically valid steady-state solutions for the flow and temperature fields, corresponding to opposite directions of circulation. These symmetric scenarios are obtained, numerically, by introducing a very small perturbation to the inclination angle ϕ, either slightly positive or slightly negative; i.e. $\phi = 0^\circ = +(10^{-12})^\circ$ or $\phi = 0^\circ = -(10^{-12})^\circ$, respectively. This perturbation determines the orientation of the resulting circulation and selects one of the two symmetric steady states. To illustrate this, solutions for the slightly positive angle are shown in the figures in black and red, while those for the slightly negative angle are shown in blue and magenta. This symmetry is further confirmed by the values of ψ_c, which display a mirror image about the abscissa ($\psi_c = 0$) of the ψ_c versus A plane of figure 11b. Finally, the same

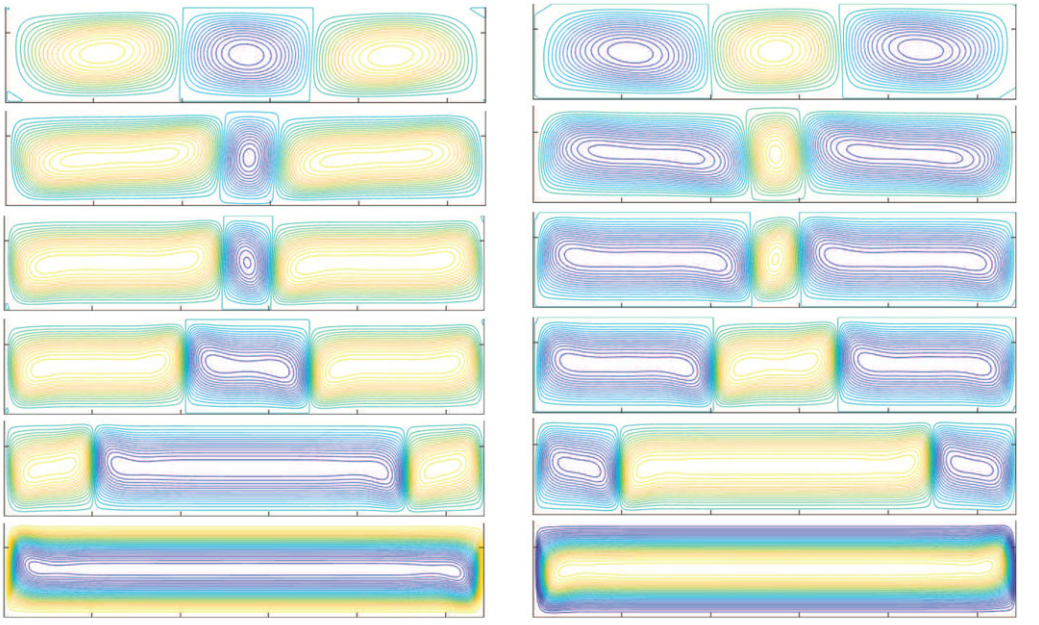

(a) Streamlines for symmetric solution with a slight positive perturbation from $\phi = 0$.

(b) Streamlines for symmetric solution with a slight negative perturbation from $\phi = 0$.

Figure 12. Convection cells for different values of A and $\phi = 0^\circ$. From top to bottom: $A = 3$, $A = 6$, $A = 10$, $A = 12$, $A = 14$, $A = 15$. Path of increasing A. Counterclockwise flow (yellow/green; lighter colour represents higher value) and clockwise flow (blue; darker colour represents higher value).

results are qualitatively illustrated in terms of the fluid streamlines and isotherms across the entire system, respectively, for specific values of the aspect ratio A, in figures 12–15.

From figure 11a–c, it is possible to observe that the two paths of increasing- versus decreasing-A, for $\phi = 0^\circ$, are different. By starting with an enclosure of aspect ratio $A = 3$, figure 11a shows that three convection cells have developed (cf. figures 2, 12 and 13). As A increases systematically from $A = 3$ to $A = 14$, the number of convection patterns in the corresponding enclosures remains constant. However, as the aspect ratio reaches $A = 15$, the three-cell circulation coalesces into a single layout, which remains stable for enclosures with values of the aspect ratio in the range of $15 \leq A \leq 20$. Conversely, by starting with an enclosure of aspect ratio $A = 20$, the computations generate a solution with 21 convection cells (cf. figures 14 and 15). As the aspect ratio decreases consistently from $A = 20$ to a value of $A = 17$, the number of convection patterns decreases, progressively, in an exponential-like fashion to a value of $N_{\text{cells}} = 3$, which remains present for enclosures with aspect ratios ranging from $A = 17$ to $A = 14$. For the aspect ratio of $A = 13$, seemingly a transition point, only two convection structures are generated, and further decrease in A, from $A = 12$ to $A = 3$, brings about only a single circulation cell. The fact that the two paths provide different results is somehow expected since the final number of circulation patterns in each path taken is a function not only of the geometrical parameter A, of the enclosure, but also of the initial conditions used in each computation.

On the other hand, from figure 11b, showing ψ_c versus A, it is seen that, in the case of increasing A, for $3 \leq A \leq 12$, the absolute value of the stream function $|\psi_c|$ changes in a decreasing-increasing-decreasing manner, in the range $|\psi_c| \in [9.7, 12.9]$. However, as the aspect ratio increases from $A = 13$ to $A = 20$, the stream function converges to $|\psi_c| = 12.9$, with insignificant variations. When the path is that of decreasing A, the figure displays a completely different trend. For instance, as A decreases from $A = 20$ to $A = 18$, a considerable change in the value of ψ_c, of approximately 24 units, is observed. In fact, the actual values of ψ_c, at $A = 18$, clearly show a complete reversal in the circulation of the flow at the centre of the enclosure, either from

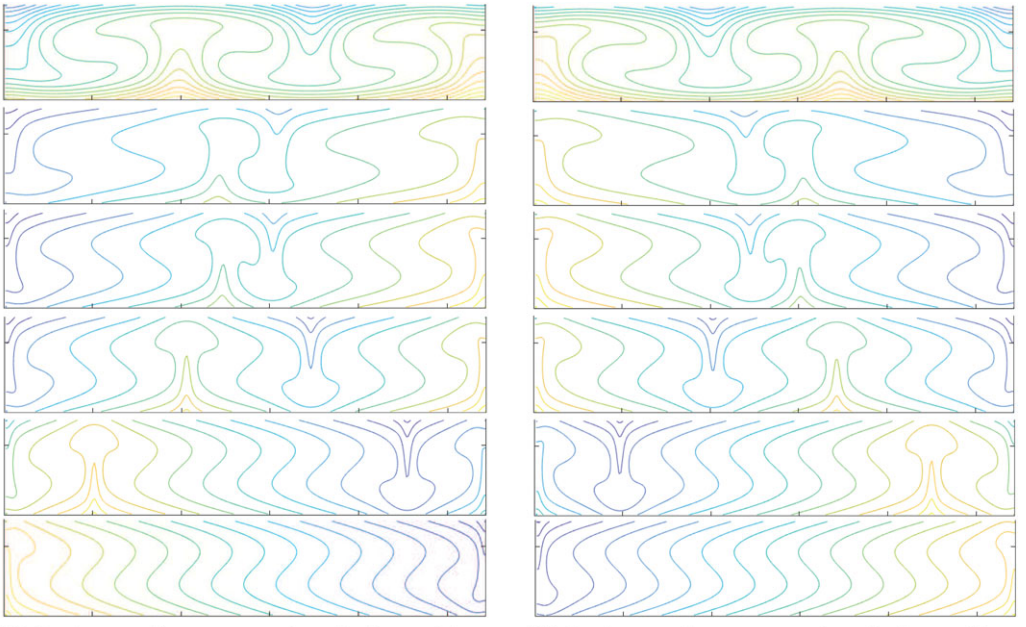

(a) Isotherms for symmetric solution with a slight positive perturbation from $\phi = 0$.

(b) Isotherms for symmetric solution with a slight negative perturbation from $\phi = 0$.

Figure 13. Convection cells for different values of A and $\phi = 0^\circ$. From top to bottom: $A = 3$, $A = 6$, $A = 10$, $A = 12$, $A = 14$, $A = 15$. Path of increasing A. Lighter colour represents higher value; darker colour represents lower value.

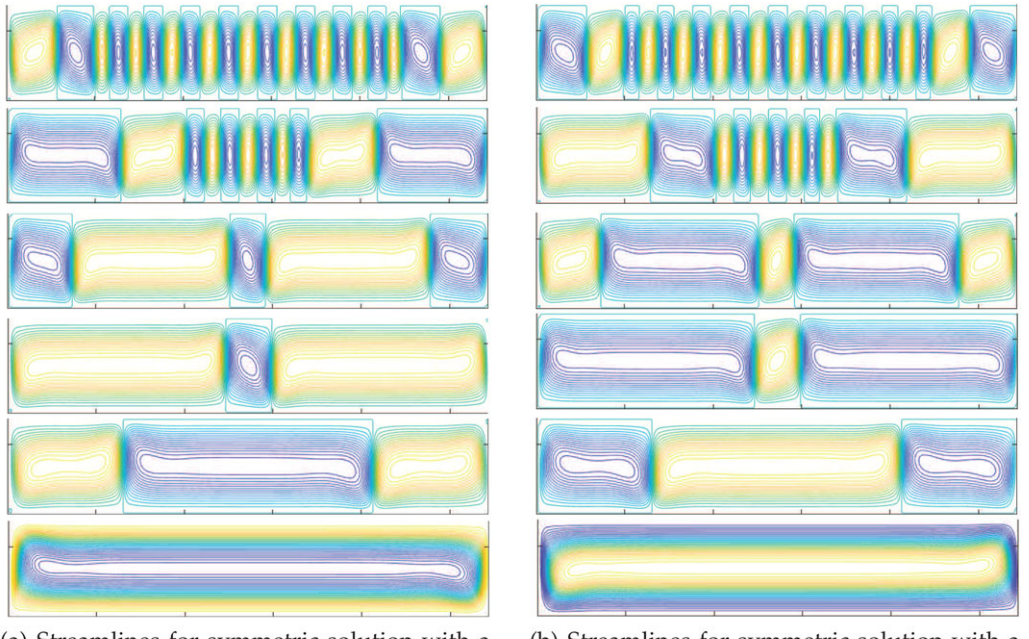

(a) Streamlines for symmetric solution with a slight positive perturbation from $\phi = 0$.

(b) Streamlines for symmetric solution with a slight negative perturbation from $\phi = 0$.

Figure 14. Convection cells for different values of A and $\phi = 0^\circ$. From top to bottom: $A = 20$, $A = 19$, $A = 18$, $A = 17$, $A = 14$, $A = 12$. Path of decreasing A. Counterclockwise flow (yellow/green; lighter colour represents higher value) and clockwise flow (blue; darker colour represents higher value).

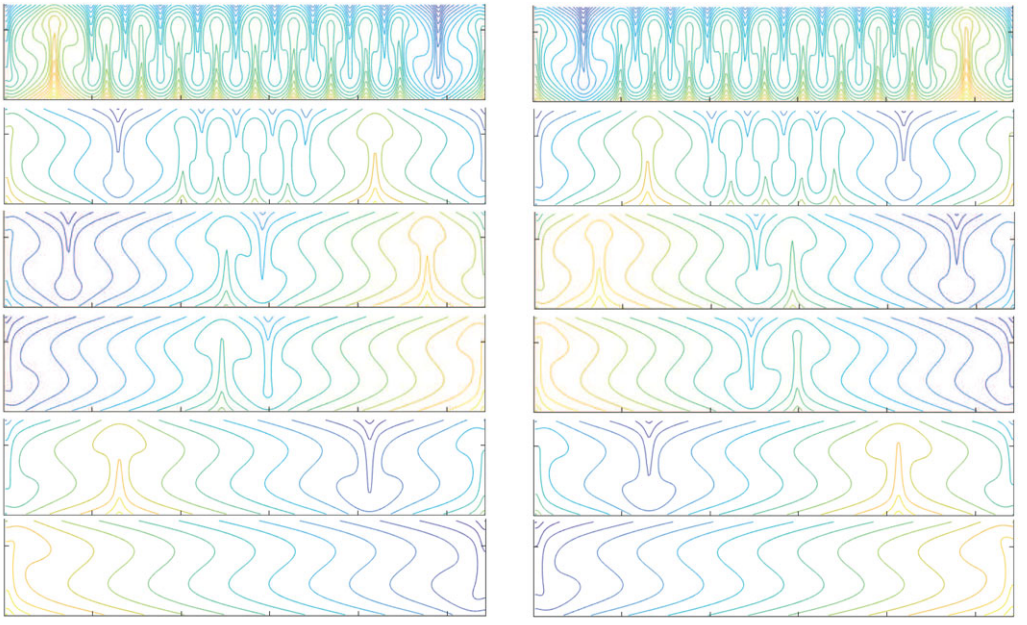

(a) Isotherms for symmetric solution with slight positive perturbation of $\phi = 0$.

(b) Isotherms for symmetric solution with slight negative perturbation of $\phi = 0$.

Figure 15. Convection cells for different values of A and $\phi = 0°$. From top to bottom: $A = 20, A = 19, A = 18, A = 17, A = 14, A = 12$. Path of decreasing A. Lighter colour represents higher value; darker colour represents lower value.

counterclockwise to clockwise rotation, or *vice versa*, from that occurring at both $A = 19$ and $A = 20$. As the aspect ratio is sequentially decreased from $A = 18$ to $A = 3$, the stream function remains at an average value of $\psi_c = \pm 12.95$, with very small variations. Similar tendencies can be observed in figure 11c for the Nusselt number Nu, at the vertical centreline of the enclosure, which varies substantially for $3 \leq A \leq 12$, for increasing-A, and $16 \leq A \leq 20$, for decreasing-A, respectively, then slowly converging to a single value of $Nu = 3.23$, averaged over the range $Nu \in [3.15, 3.3]$, for all remaining values of A, along the two paths.

Further attention to figure 11a–c enables identifying relative agreement between the number of convection cells N_{cells}, developed for each enclosure, and the variability of both ψ_c and Nu. From figure 11b,c, for instance, it can be noticed that, regardless of the path taken for A, if $N_{\text{cells}} = 1$, then both ψ_c and Nu are relatively constant (at values around 12.9 and 3.23, respectively). However, regardless of A, wide variations in both ψ_c and Nu are seen for $N_{\text{cells}} > 1$, the exception being the range $12 \leq A \leq 16$, which seems to constitute a set of transition points. Finally, it is important to note that though the information in the figures provides a good idea of the convective behaviour of the fluid inside the set of enclosures considered, it does not completely describe it since, regardless of the number of circulation patterns present, the trend in the Nusselt number Nu, which roughly follows that of the stream function ψ_c, for most values of A in the domain differs substantially within the transition range mentioned above. Thus, additional information, on the number of circulation cells N_{cells} and their relative size, seem to also play a role. This is discussed further below.

A qualitative account of the numerical solutions discussed above is provided in terms of both streamlines and isotherms in figures 12–15 to illustrate the evolution in the number of circulation structures and their relative size, using enclosures of specific aspect ratios. Figures 12 and 13 show the data for $A = \{3, 6, 10, 12, 14, 15\}$, for the path of increasing A, while figures 14 and 15 illustrate the results for $A = \{20, 19, 18, 17, 14, 12\}$, for the path of decreasing A. Though not included here, results for other values of aspect ratio A and Rayleigh number Ra have shown similar qualitative behaviour. Note that in the case of the streamlines displayed in figures 12

and 14, lighter colour represents a higher positive value, while darker colour represents a higher *negative* value. In addition, positive values of ψ are indicative of counterclockwise flow, while negative ones represent clockwise circulation. On the other hand, for the isotherms shown in figures 13 and 15, lighter colour represents a higher value of temperature, while darker colour represents a lower temperature. Furthermore, although the figures are not up to scale, their information still gives a good sense of the dynamics of the convection patterns as functions of the aspect ratio. Finally, the symmetry of the problem, as discussed earlier in detail, is further demonstrated in figures 12–15, for both the streamlines and isotherms. These results correspond to the two symmetric steady-state solutions associated with opposite directions of circulation, obtained through independent computations using slight positive or negative perturbations of the inclination angle $\phi = 0$. For clarity and consistency, figures 12a–15a present one of the symmetric solutions, while figures 12b–15b show the other. Since the two solutions are physically equivalent, the discussion will focus on the results corresponding to the configuration shown in figures 12a–15a.

Let us first focus on the evolution of the circulation cells for the path of increasing A, for which figures 12a–13a show that, starting from rest and a conductive thermal field, an enclosure with $A = 3$ develops three convection cells of roughly equal size—two rotating counterclockwise and one clockwise at the centre. The isotherms closely follow this pattern, revealing that the temperature distribution includes two plume-like structures at the merging lines of the convective fluid rotations. Importantly, as expected for $\phi = 0$, the circulation structures are symmetric for the streamlines and anti-symmetric for the isotherms, with respect to the vertical centreline of the enclosure. As the aspect ratio increases from $A = 3$ to $A = 14$, the number of cells remains unchanged, consistent with the results of figure 11a, but their sizes evolve. For instance, from $A = 3$ to $A = 6$, the central cell shrinks while the side cells enlarge. However, with further increases in A to 10, 12 and 14, the trend reverses—the middle cell grows and merges with the outer cells, eventually forming a single structure for $A \in [15, 20]$. Additional calculations (not shown here but to be reported elsewhere) highlight key observations. First, although the initial reduction in the central convective cell at $A = 6$ accounts for less than 20% of its original size, its subsequent growth exceeds this reduction by 33%, and then follows it with an exponential trend in size until a single circulation fills the entire enclosure. Second, the isotherms reflect these changes, as the plumes gradually shift away from the centreline and weaken with increasing A, and by $A = 14$, they disappear, producing a nearly stratified temperature field. This transition corresponds to variations in ψ_c and Nu, as shown in figure 11b,c, for $3 \leq A \leq 14$. Finally, the merging of the central and side convection cells occurs in the manner discussed above because the central flow circulation is stronger and more stable, since it is sustained by the circulation of the side cells, whereas the side convective patterns weaken due to shear stresses at the walls, which slow down the flow until it is overtaken by the dominant central circulation. The single convective cell observed for $15 \leq A \leq 20$ appears to be a highly stable steady-state condition, as indicated by the constant values of ψ_c and Nu, in figure 11b,c.

Now the focus is on the evolution of the circulation cells for the path of decreasing A, for which figures 14a–15a portray a completely different story. Beginning from rest and a conduction thermal field, the enclosure of $A = 20$ develops 21 convection cells (cf. figures 11a and 14a), resembling the well-known Rayleigh–Benard convection patterns. Approximately half of these cells, which are of similar size, except for the two pairs near the sidewalls, rotate counterclockwise, while the others rotate clockwise. As before, the isotherms in figure 15a clearly illustrate the temperature distribution, revealing 20 plume-like structures along the merging lines of adjacent convection patterns. In addition, the circulation structures are symmetric for the streamlines and anti-symmetric for the isotherms with respect to the vertical centreline of the enclosure. When the aspect ratio decreases to $A = 19$, a coalescence process begins, reducing the number of cells to $N_{\text{cells}} = 11$. This reduction occurs as the two outermost cells merge into larger structures, while the adjacent set of five cells also combine into a single circulation. In addition, the central convection patterns remain unchanged. At $A = 18$, the number of fluid rotations further decreases to $N_{\text{cells}} = 5$ due to the fact that not only do the five central cells emerge into a single structure

but also the adjacent rotation patterns expand and progressively merge into the outer cells, which disappear entirely by $A = 17$, leaving only three circulation structures. Between $A = 17$ and $A = 14$, these three flow rotations persist but undergo continuous size adjustments; the central cell enlarges, while the side cells shrink, ultimately coalescing into a single structure for $A \in [3, 12]$. The temperature field reflects these changes, with isothermal plumes decreasing in number while expanding in size. Eventually, only two plumes remain and shift away from the centreline, weakening as A decreases. By $A = 12$, the initially complex isothermal structures have decayed into a stable, stratified temperature field.

It is important to note that, as previously discussed, the flow circulation structures farther from the lateral walls and closer to the centre of the enclosure exhibit greater strength and stability compared to those near the sidewalls. This directly influences the number and size of the convection cells as the aspect ratio decreases. For instance, figure 14a illustrates that for enclosures with aspect ratios ranging from $A = 17$ to $A = 3$, the stronger central flow circulation eventually overtakes the weaker adjacent outer flow rotations and expands until it fills the entire enclosure. The strength of this central convection cell is corroborated by the results of figure 11b,c, which show approximately constant values for both ψ_c and Nu. However, the isotherms of figure 15a, for $A = 17$, indicate that the energy transfer remains in progress, as the two plumes are still positioned very close to each other. From $A = 20$ to $A = 19$, $A = 18$ and finally to $A = 17$, the same mechanism governs the coalescence of the two outermost cells, which merge into a larger structure. In each case, the stronger convective rotation eventually overtakes the weaker one, a behaviour evident in the way the newly formed convection structure adopts the rotational direction of the dominant cell. According to the figures, for $A = 19$, the resulting circulation closest to the wall rotates clockwise. At $A = 18$, this convection cell initially shrinks and then transitions into a counterclockwise rotation at $A = 17$. A similar pattern occurs in the circulation structures adjacent to those near the wall, with the added effect that the number of cells rotating in one direction exceeds those rotating in the opposite direction. This imbalance facilitates the merging process in favour of the stronger circulation patterns. For $A = 19$, a set of three counter-rotating and two co-rotating cells present at $A = 20$ merge into a single larger counter-rotating circulation. Similarly, at $A = 18$, the central co-rotating fluid circulation results from the coalescence of a set of four co-rotating and three counter-rotating cells, including the one at the centre of the cavity, originally present at $A = 19$. These observations help explain the drastic variations in both ψ_c and Nu, in figure 11b,c, for $A = \{20, 19, 18, 17\}$, as previously discussed.

6. Concluding remarks

Thermal natural convection in enclosures plays a fundamental role in a broad range of engineering and environmental applications, and a complete knowledge of its underlying fluid transport mechanisms is necessary since they have significant influence on design considerations and the operational performance of related devices and equipment. Over the past six decades, extensive research has been conducted to develop an understanding about the complex features of natural convection in these systems using analytical and numerical techniques for various geometries, including the inclined, slender, rectangular design. Despite significant advancements, most studies on slender enclosures have focused on unicellular convective motion, providing valuable insights into the multiplicity and stability of the corresponding solutions. However, strong interplay among geometry, boundary conditions and inclination angle, in these configurations, introduces significant complexity, often giving rise to intricate and unexpected flow patterns.

In the present work, we have considered the analysis of the fluid flow and heat transfer characteristics of thermal natural convection, of air, in slender, inclined enclosures, with emphasis on the existence of uni- and multi-cellular steady states. By implementing an integrated approach based on the traditional parallel-flow approximation, along with comprehensive finite difference simulations of the two-dimensional governing equations, the influence of inclination angle and aspect ratio on the emergence of multiple solutions, and the transitions between different flow

regimes, has been examined in detail, for inclination angles in the range $-180^\circ < \phi < 180^\circ$, aspect ratios in $3 \leq A \leq 20$ and Rayleigh numbers in the range $720 \leq Ra \leq 10^5$.

Using the procedure, along with the concepts of stream function at the centre of the enclosure ψ_c and the Nusselt number Nu at the vertical centreline, supplemented by detailed accounts of the flow and temperature fields, the results indicate that multiple steady states, either unicellular and/or multi-cellular, are possible within specific inclination angles, aspect ratios and Rayleigh numbers above the critical. From a mathematical perspective, these results highlight the nonlinear nature not only of the incompressible fluid mechanics equations but also of the natural convection process itself and demonstrates the crucial role of the initial conditions in determining the final state of the system. In addition, the inherent symmetry of the governing equations is demonstrated by the resulting values of ψ_c and Nu, and the flow and temperature patterns, which, from a physical perspective, represent two symmetric, physically valid steady-state solutions corresponding to opposite directions of circulation. This symmetry is an intrinsic property of the system and is entirely independent of the position of an observer standing either in front of or behind the enclosure.

The results for an enclosure of fixed aspect ratio (in the present case, $A = 4$) and varying inclination angle ϕ confirm what other investigations have reported in the past for this and similar systems; i.e. that for Rayleigh numbers above the critical value, multiple steady states exist within a specific range of ϕ around the horizontal configuration, whereas outside this range, only one steady-state solution—corresponding to unicellular circulation—is possible. However, for a horizontal configuration, depending on the initial conditions, the present results show that either unicellular or multi-cellular circulations, of which the three-cellular solution is the *natural* condition, is possible. It is to note that this *natural* versus *antinatural* motion/condition is referred in this way depending on whether the steady-state solution is obtained by starting—respectively—from a conduction temperature field with the fluid being at rest or not. On the other hand, for a horizontal enclosure ($\phi = 0$) and varying aspect ratio A, with a Rayleigh number well above the critical value, the results from this analysis demonstrate that two distinct pathways are possible, revealing significant differences in the steady-state solutions, which depend not only on the enclosure geometry but also on the initial conditions. The results demonstrate that, along the path of increasing A, an initial three-cell convection structure collapses into a single large circulation. Conversely, for the path of decreasing A, a system starting with a solution with 21 convection cells, progressively coalesce into larger structures, eventually stabilizing into a single convective circulation. The observed differences between the two paths highlight the existence of hysteresis, where the final convection pattern depends on the sequence of changes in the aspect ratio rather than exclusively on the geometric configuration.

Furthermore, the solutions presented here demonstrate that, regardless of the path taken for aspect ratio, the values of ψ_c and Nu correlate strongly with the number of resulting convection cells and their relative size, with significant fluctuations occurring during transitions between different circulation patterns. The qualitative analysis of streamlines and isotherms further confirms that the dominant convection structure results from the competition between stronger central cells and weaker peripheral ones, ultimately determining the stability of the flow. Finally, the fact that both unicellular and multi-cellular solutions were reached using a time marching technique is numerical evidence of the linear stability of the results. Thus, whenever linearly stable multiple steady states are possible, the final solution is determined uniquely by the initial conditions. If the basin of attraction of any linearly stable steady-state solution is sufficiently large, then the initial conditions leading to it can then be found, and this will be pursued and reported in the future.

Data accessibility. The code (in MATLAB) used for the simulations is included as electronic supplementary material [50].

Declaration of AI use. We have not used AI-assisted technologies in creating this article.

Authors' contributions. A.P.V.: conceptualization, formal analysis, funding acquisition, investigation, methodology, validation, visualization and writing—original draft; M.S.: conceptualization, formal analysis, investigation, methodology and writing—original draft.

Both authors gave final approval for publication and agreed to be held accountable for the work performed therein.

Conflict of interest declaration. We declare we have no competing interests.

Funding. This work has been partially supported by the National Science Foundation with award nos. HRD-1547723 and HRD-2112554.

Appendix A

(a) Natural solution ($C \sin\phi > 0$)

Integration of equation (4.3*a*) gives rise to

$$\psi(y) = c_1 \cos ey \cosh ey + c_2 \cos ey \sinh ey + c_3 \sin ey \cosh ey + c_4 \sin ey \sinh ey + \frac{1 + C\cot\phi}{C}, \tag{A 1}$$

and, by using the boundary conditions equations (4.5), the above constants become

$$c_1 = -\frac{(1 + C\cot\phi)(\sin(e/2)\cosh(e/2) + \cos(e/2)\sinh(e/2))}{C(\sin(e/2)\cos(e/2) + \sinh(e/2)\cosh(e/2))}, \quad c_2 = 0 \tag{A 2a}$$

and

$$c_3 = 0, \quad c_4 = \left(\frac{\sin(e/2)\cosh(e/2) - \cos(e/2)\sinh(e/2)}{\sin(e/2)\cosh(e/2) + \cos(e/2)\sinh(e/2)}\right) c_1. \tag{A 2b}$$

The final solution is then given by equation (4.8) of §4b(i). Using a similar process, integration of equation (4.3*b*) leads to

$$\eta(y) = C \int \psi(y)\, dy + c_5 y + c_6. \tag{A 3}$$

By applying conditions equation (4.6) and (4.7), the constants become $c_5 = -1$ and $c_6 = 0$. The final solution for $\eta(y)$ is equation (4.10) of §4b(i).

(b) Antinatural solution ($C \sin\phi < 0$)

For the case in which $C \sin\phi \leq 0$, integration of equation (4.3*a*) gives rise to

$$\psi(y) = c_1 \cos by + c_2 \sin by + c_3 \cosh by + c_4 \sinh by + \frac{1 + C\cot\phi}{C}. \tag{A 4}$$

By using the same boundary conditions equation (4.5), as in the previous case, the above constants become

$$c_1 = -\frac{(1 + C\cot\phi)(\sinh(b/2))}{C(\sin(b/2)\cosh(b/2) + \cos(b/2)\sinh(b/2))}, \quad c_2 = 0 \tag{A 5a}$$

and

$$c_3 = \frac{\sin(b/2)}{\sinh(b/2)}\, c_1, \quad c_4 = 0, \tag{A 5b}$$

with the final solution being now equation (4.13) of §4b(ii). As in the previous section, integration of equation (4.3*b*) leads to

$$\eta(y) = C \int \psi(y)\, dy + c_5 y + c_6, \tag{A 6}$$

where by applying conditions equation (4.6) and (4.7), the constants obtain the values $c_5 = -1$ and $c_6 = 0$. Again, the final solution of $\eta(y)$ is equation (4.15) of §4b(ii).

(c) Horizontal enclosure ($\phi = 0$)

In this specific case, the model equations (4.3*d*) and (4.3*b*), along with the boundary conditions, reduce to

$$\frac{\mathrm{d}^4\psi}{\mathrm{d}y^4} = RaC; \quad \psi(\pm 1/2) = 0; \quad \frac{\mathrm{d}\psi}{\mathrm{d}y}(\pm 1/2) = 0; \tag{A 7a}$$

and

$$\frac{\mathrm{d}^2\eta}{\mathrm{d}y^2} - C\frac{\mathrm{d}\psi}{\mathrm{d}y} = 0; \quad \eta(0) = 0; \quad \left.\frac{\mathrm{d}\eta}{\mathrm{d}y}\right|_{1/2} = -1. \tag{A 7b}$$

The solutions are now simple polynomials, given as

$$\psi(y) = RaC\frac{y^4}{24} + c_1\frac{y^3}{6} + c_2\frac{y^2}{2} + c_3 y + c_4 \tag{A 8}$$

and

$$\eta(y) = \frac{RaC^2}{24}\left(\frac{y^5}{5} - \frac{y^3}{6}\right) + c_5 y + c_6, \tag{A 9}$$

with the following values for the constants:

$$c_1 = 0; \quad c_2 = -\frac{RaC}{24}; \quad c_3 = 0; \quad c_4 = \frac{RaC}{384}; \quad c_5 = \frac{RaC^2}{384} - 1; \quad c_6 = 0.$$

From these, the final solutions are

$$\psi(y) = \frac{RaC}{24}\left(y^4 - \frac{y^2}{2} + \frac{1}{16}\right) \tag{A 10}$$

and

$$\eta(y) = \frac{RaC^2}{24}\left(\frac{y^5}{5} - \frac{y^3}{6} + \frac{1}{16}\right) - y. \tag{A 11}$$

By substituting equations (A 10) and (A 11) into condition equation (4.4), we obtain the equation for C, from which the constant C can be written explicitly as

$$C = 0 \quad \text{or} \quad C = \pm\frac{6}{Ra}\sqrt{14(Ra - 720)}, \tag{A 12}$$

thus leading to explicit expressions for both ψ_c and Nu:

$$\psi_c = \frac{RaC}{384} \quad \text{and} \quad Nu = \frac{720}{720 - RaC^2}. \tag{A 13}$$

(d) Vertical cavity ($\phi = 90^\circ$)

In the case of $\phi = 90^\circ$, equations (4.3*a*) and (4.3*b*), along with the boundary conditions equations (4.5), (4.6) and (4.7), reduce to

$$\frac{\mathrm{d}^4\psi}{\mathrm{d}y^4} + Ra\frac{\mathrm{d}\eta}{\mathrm{d}y} = 0; \quad \psi(\pm 1/2) = 0; \quad \frac{\mathrm{d}\psi}{\mathrm{d}y}(\pm 1/2) = 0 \tag{A 14a}$$

and

$$\frac{\mathrm{d}^2\eta}{\mathrm{d}y^2} - C\frac{\mathrm{d}\psi}{\mathrm{d}y} = 0; \quad \eta(0) = 0; \quad \left.\frac{\mathrm{d}\eta}{\mathrm{d}y}\right|_{1/2} = -1, \tag{A 14b}$$

for which the general solution for ψ is

$$\psi(y) = c_1 \cos ey \cosh ey + c_2 \cos ey \sinh ey + c_3 \sin ey \cosh ey + c_4 \sin ey \sinh ey. \tag{A 15}$$

By using the above boundary conditions, the constants become

$$c_1 = -\frac{(\sin(e/2)\cosh(e/2) + \cos(e/2)\sinh(e/2))}{C(\sin(e/2)\cos(e/2) + \sinh(e/2)\cosh(e/2))}, \quad c_2 = 0 \tag{A 16a}$$

and

$$c_3 = 0, \quad c_4 = \left(\frac{\sin(e/2)\cosh(e/2) - \cos(e/2)\sinh(e/2)}{\sin(e/2)\cosh(e/2) + \cos(e/2)\sinh(e/2)} \right) c_1, \tag{A 16b}$$

thus leading to the final solution for $\psi(y)$ as

$$\psi(y) = -\frac{P_B}{2e} \left[(1-\epsilon) \left\{ \sin\frac{e}{2}\sinh\frac{e}{2} - \sin ey \sinh ey \right\} + (1+\epsilon) \left\{ \cos\frac{e}{2}\cosh\frac{e}{2} - \cos ey \cosh ey \right\} \right]. \tag{A 17}$$

Following the processes outlined in the previous sections of this appendix, the solution to the energy equation and the boundary conditions of equations (A 14*d*) and (A 14*b*) is

$$\eta(y) = C \int \psi(y) dy + c_5 y + c_6, \tag{A 18}$$

with $c_5 = -1$ and $c_6 = 0$. The final expression for $\eta(y)$ is

$$\eta(y) = \frac{CP_B}{2e^2} \{ \sin ey \ \cosh ey + \epsilon \cos ey \sinh ey \}. \tag{A 19}$$

In the aforementioned solutions, the constants e, ϵ and P_B are, respectively,

$$e = \left(\frac{Ra\, C}{4} \right)^{1/4}; \quad \epsilon = \cot\frac{e}{2}\tanh\frac{e}{2} \tag{A 20a}$$

and

$$P_B = -\frac{2e}{C\{(1+\epsilon)\cos(e/2)\cosh(e/2) + (1-\epsilon)\sin(e/2)\sinh(e/2)\}}. \tag{A 20b}$$

Again, an equation for the constant C is given by the condition equation (4.4) as

$$\frac{CP_B^2}{16e^3} \left[(\epsilon^2 + 2\epsilon - 1)\cos e \sinh e + (-\epsilon^2 + 2\epsilon + 1)\sin e \cosh e \right] - \frac{\epsilon CP_B^2}{4e^2} - C = 0. \tag{A 21}$$

The transcendental equations (A 20*d*), (A 20*b*) and (A 21) have to be simultaneously solved again for the unknowns e, P_B and C, using the Newton–Raphson scheme. It is always possible to find real values of the constants for any Ra and ϕ. The stream function and temperature fields are then known from equations (A 17) and (A 19).

References

1. Ostrach S. 1988 Natural convection in enclosures. *ASME J. Heat Transfer.* **110**, 1175–1189. (doi:10.1115/1.3250619)
2. Bairi A, Zarco-Pernia E, de Maria JMG. 2014 A review on natural convection in enclosures for engineering applications. The particular case of the parallelogrammic diode cavity. *Appl. Therm. Eng.* **63**, 304–322. (doi:10.1016/j.applthermaleng.2013.10.065)
3. Das D, Roy M, Basak T. 2017 Studies on natural convection within enclosures of various (non-square) shapes—a review. *Int. J. Heat Mass Transfer* **106**, 356–406. (doi:10.1016/j.ijheatmasstransfer.2016.08.034)
4. Fan Y, Zhao Y, Torres J, Xu F, Lei CW, Li Y, Carmeliet J. 2021 Natural convection over vertical and horizontal heated flat surfaces: a review of recent progress focusing on underpinnings and implications for heat transfer and environmental applications. *Phys. Fluids* **33**, 101301. (doi:10.1063/5.0065125)
5. Awbi H, Hatton A. 1999 Natural convection from heated room surfaces. *Energy Build.* **30**, 233–244. (doi:10.1016/S0378-7788(99)00004-3)
6. Zhao FY, Liu D, Tang G. 2008 Multiple steady fluid flows in a slot-ventilated enclosure. *Int. J. Heat Fluid Flow* **29**, 1295–1308. (doi:10.1016/j.ijheatfluidflow.2008.06.005)
7. Bairi A, Bauzin JG, Martin-Garin A, Alilat N, Millan-Garcia J. 2019 Natural convective cooling of electronics contained in tilted hemispherical enclosure filled with a porous medium saturated by water-copper nanofluid. *Int. J. Numer. Methods Heat Fluid Flow* **29**, 280–293. (doi:10.1108/HFF-01-2018-0036)

8. Laguerre O, Remy D, Flick D. 2009 Airflow, heat and moisture transfers by natural convection in a refrigerating cavity. *J. Food Eng.* **91**, 197–210. (doi:10.1016/j.jfoodeng.2008.08.029)
9. Mavromatidis L. 2016 Study of coupled transient radiation-natural convection heat transfer across rectangular cavities in the vicinity of low emissivity thin films for innovative building envelope applications. *Energy Build.* **120**, 114–134. (doi:10.1016/j.enbuild.2016.03.053)
10. Sheremet M, Pop I, Mahian O. 2018 Natural convection in an inclined cavity with time-periodic temperature boundary conditions using nanofluids: application in solar collectors. *Int. J. Heat Mass Transfer* **116**, 751–761. (doi:10.1016/j.ijheatmasstransfer.2017.09.070)
11. Batchelor G. 1954 Heat transfer by free convection across a closed cavity between vertical boundaries at different temperatures. *Quart. Appl. Math.* **12**, 209–233. (doi:10.1090/qam/64563)
12. Sparrow E, Goldstein R, Jonsson V. 1964 Thermal instability in a horizontal fluid layer: effect of boundary conditions and non-linear temperature. *J. Fluid Mech.* **18**, 513–528. (doi:10.1017/S0022112064000386)
13. Gill A. 1966 The boundary-layer regime for convection in a rectangular cavity. *J. Fluid Mech.* **26**, 515–536. (doi:10.1017/S0022112066001368)
14. Cormack D, Leal L, Imberger J. 1974 Natural convection in a shallow cavity with differentially heated end walls. Part 1. Asymptotic theory. *J. Fluid Mech.* **65**, 209–229. (doi:10.1017/S0022112074001352)
15. Cormack D, Stone G, Leal L. 1975 The effect of upper surface conditions on convection in a shallow cavity with differentially heated end-walls. *J. Fluid Mech.* **18**, 635–648. (doi:10.1016/0017-9310(75)90275-6)
16. Walker K, Homsy G. 1978 Convection in a porous cavity. *J. Fluid Mech.* **87**, 449–474. (doi:10.1017/S0022112078001718)
17. de Vahl Davis G. 1968 Laminar natural convection in an enclosed rectangular cavity. *Int. J. Heat Mass Transfer* **11**, 1675–1693. (doi:10.1016/0017-9310(68)90047-1)
18. Catton I, Ayyaswamy P, Clever R. 1974 Natural convection flow in a finite, rectangular slot arbitrarily oriented with respect to the gravity vector. *Int. J. Heat Mass Transfer* **17**, 173–184. (doi:10.1016/0017-9310(74)90079-9)
19. Cormack D, Leal L, Seinfeld J. 1974 Natural convection in a shallow cavity with differentially heated end walls. Part 2. Numerical solutions. *J. Fluid Mech.* **65**, 231–246. (doi:10.1017/S0022112074001364)
20. Gilly B, Bontoux P, Roux B. 1981 Influence of thermal wall conditions on the natural convection in a vertical rectangular differentially heated cavity. *Int. J. Heat Mass Transfer* **24**, 829–841. (doi:10.1016/S0017-9310(81)80006-3)
21. Salmun H. 1995 Convection patterns in a triangular domain. *Int. J. Heat Mass Transfer* **38**, 351–362. (doi:10.1016/0017-9310(95)90029-2)
22. Diaz G, Winston R. 2008 Effect of surface radiation on natural convection in parabolic enclosures. *Numer. Heat Transfer Part A: Appl.* **53**, 891–906. (doi:10.1080/10407780701789518)
23. Geridonmez B, Oztop H. 2019 Natural convection in a cavity filled with porous medium under the effect of a partial magnetic field. *Int. J. Mech. Sci.* **161–162**, 105077. (doi:10.1016/j.ijmecsci.2019.105077)
24. Lefauve A, Linden P. 2020 Buoyancy-driven exchange flows in inclined ducts. *J. Fluid Mech.* **893**, A2. (doi:10.1017/jfm.2020.212)
25. Ferialdi H, Lappa M, Haughey C. 2020 On the role of thermal boundary conditions in typical problems of buoyancy convection: a combined experimental-numerical analysis. *Int. J. Heat Mass Transfer* **159**, 120012. (doi:10.1016/j.ijheatmasstransfer.2020.120012)
26. Hart J. 1971 Stability of the flow in a differentially heated inclined box. *J. Fluid Mech.* **47**, 547–576. (doi:10.1017/S002211207100123X)
27. Creveling H, Paz JD, Baladi J, Schoenhals R. 1975 Stability characteristics of a single-phase free convection loop. *J. Fluid Mech.* **67**, 65–84. (doi:10.1017/S0022112075000171)
28. Ozoe H, Yamamoto K, Sayama H, Churchill S. 1977 Natural convection patterns in a long inclined rectangular box heated from below. *Int. J. Heat Mass Transfer* **20**, 131–139. (doi:10.1016/0017-9310(77)90004-7)
29. Wirtz R, Tseng WF. 1979 Free convection across tilted enclosures of low aspect ratio. *Bull. Am. Phys. Soc.* **24**, 1135.
30. Ostrach S. 1982 Natural convection heat transfer in cavities and cells. In *International heat transfer conference digital library, Munich, Germany, 6–10 September* (doi:10.1615/ihtc7.4400). Begel House Inc.

31. Kimura S, Bejan A. 1984 The boundary layer natural convection regime in a rectangular cavity with uniform heat flux from the side. *ASME J. Heat Transfer* **106**, 98–103. (doi:10.1115/1.3246666)
32. Sen M, Ramos E, Trevino C. 1985 On the steady-state velocity of the inclined toroidal thermosyphon. *ASME J. Heat Transfer* **107**, 974–977. (doi:10.1115/1.3247533)
33. Acosta R, Sen M, Ramos E. 1987 Single-phase natural circulation in a tilted square loop. *Wärme- und Stoffübertragung* (now Heat Mass Transfer) **21**, 269–275.
34. Moya S, Ramos E, Sen M. 1987 Numerical study of natural convection in a tilted rectangular porous material. *Int. J. Heat Mass Transfer* **30**, 741–756. (doi:10.1016/0017-9310(87)90204-3)
35. Yang K. 1988 Transitions and bifurcations in laminar buoyant flows in confined enclosures. *ASME J. Heat Transfer* **110**, 1191–1204. (doi:10.1115/1.3250620)
36. Guerrero-Martinez F, Karimi N, Ramos E. 2018 Numerical modeling of multiple steady-state convective modes in a tilted porous medium heated from below. *Int. Commun. Heat Mass Transfer* **92**, 64–72. (doi:10.1016/j.icheatmasstransfer.2018.02.009)
37. Pacheco-Vega A, Franco W, Chang HC, Sen M. 2002 Nonlinear analysis of tilted toroidal thermosyphon models. *Int. J. Heat Mass Transfer* **45**, 1379–1391. (doi:10.1016/S0017-9310(01)00265-4)
38. Bejan A, Tien C. 1978 Natural convection in a horizontal porous medium subjected to an end-to-end temperature difference. *ASME J. Heat Transfer* **100**, 191–198. (doi:10.1115/1.3450780)
39. Bejan A. 1980 A synthesis of analytical results for natural convection heat transfer across rectangular enclosures. *Int. J. Heat Mass Transfer* **23**, 723–726. (doi:10.1016/0017-9310(80)90017-4)
40. Vasseur P, Robillard L, Sen M. 1987 Unicellular convective motion in an inclined fluid layer with uniform heat flux. In *Bifurcation phenomena in thermal processes and convection* (eds H Bau, L Bertram, S Korpela), HTD-vol. 94/AMD-vol. 89, pp. 23–29. Boston, MA: ASME.
41. Vasseur P, Hasnaoui M, Bilgen E. 1994 Analytical and numerical study of natural convection heat transfer in an inclined composite enclosure. *Appl. Sci. Res.* **52**, 187–207. (doi:10.1007/BF00853950)
42. Sen M, Vasseur P, Robillard L. 1987 Multiple steady states for unicellular natural convection in an inclined porous layer. *Int. J. Heat Mass Transfer* **30**, 2097–2113. (doi:10.1016/0017-9310(87)90089-5)
43. Sen M, Vasseur P, Robillard L. 1988 Parallel flow convection in a tilted two-dimensional porous layer heated from all sides. *Phys. Fluids* **31**, 3480–3487. (doi:10.1063/1.866916)
44. Vasseur P, Wang C, Sen M. 1989 The Brinkman model for natural convection in a shallow porous cavity with uniform heat flux. *Numer. Heat Transfer Part A—Appl.* **15**, 221–242. (doi:10.1080/10407788908944686)
45. Vasseur P, Wang C, Sen M. 1990 Natural convection in an inclined rectangular porous slot—the Brinkman-extended Darcy model. *ASME J. Heat Transfer* **112**, 507–511. (doi:10.1115/1.2910412)
46. Lamsaadi M, Naimi M, Hasnaoui M. 2006 Multiple steady-state solutions for natural convection in a shallow horizontal cavity filled with non-Newtonian power-law fluids and heated from all sides. *Int. J. Numer. Methods Heat Fluid Flow* **16**, 779–802. (doi:10.1108/09615530610683511)
47. Lamsaadi M, Naimi M, Bahlaoui A, Raji A, Hasnaoui M. 2007 Multiple steady-state solutions for natural convection in a tilted rectangular slot containing non-Newtonian power-law fluids and subject to a transverse thermal gradient. *Numer. Heat Transfer Part A—Appl.* **51**, 393–414. (doi:10.1080/10407780600829662)
48. Alloui Z, Vasseur P, Reggio M. 2012 Analytical and numerical study of buoyancy-driven convection in a vertical enclosure filled with nanofluids. *Heat Mass Transfer* **48**, 627–639. (doi:10.1007/s00231-011-0911-8)
49. Mallinson G, de Vahl Davis G. 1973 The method of the false transient for the solution of coupled elliptic equations. *J. Comput. Phys.* **12**, 435–461. (doi:10.1016/0021-9991(73)90097-1)
50. Pacheco-Vega A, Sen M. 2025 Analytical and numerical steady states for thermal convection in an inclined, slender, two-dimensional enclosure. Figshare. (doi:10.6084/m9.figshare.c.8012258)